Mesoscale Simulation of Blood Flow in Small Vessels

Prosenjit Bagchi
Department of Mechanical and Aerospace Engineering, Rutgers University, The State University of New Jersey, Piscataway, New Jersey

ABSTRACT Computational modeling of blood flow in microvessels with internal diameter 20–500 μm is a major challenge. It is because blood in such vessels behaves as a multiphase suspension of deformable particles. A continuum model of blood is not adequate if the motion of individual red blood cells in the suspension is of interest. At the same time, multiple cells, often a few thousands in number, must also be considered to account for cell-cell hydrodynamic interaction. Moreover, the red blood cells (RBCs) are highly deformable. Deformation of the cells must also be considered in the model, as it is a major determinant of many physiologically significant phenomena, such as formation of a cell-free layer, and the Fahraeus-Lindqvist effect. In this article, we present two-dimensional computational simulation of blood flow in vessels of size 20–300 μm at discharge hematocrit of 10–60%, taking into consideration the particulate nature of blood and cell deformation. The numerical model is based on the immersed boundary method, and the red blood cells are modeled as liquid capsules. A large RBC population comprising of as many as 2500 cells are simulated. Migration of the cells normal to the wall of the vessel and the formation of the cell-free layer are studied. Results on the trajectory and velocity traces of the RBCs, and their fluctuations are presented. Also presented are the results on the plug-flow velocity profile of blood, the apparent viscosity, and the Fahraeus-Lindqvist effect. The numerical results also allow us to investigate the variation of apparent blood viscosity along the cross-section of a vessel. The computational results are compared with the experimental results. To the best of our knowledge, this article presents the first simulation to simultaneously consider a large ensemble of red blood cells and the cell deformation.

INTRODUCTION

Blood is a multiphase fluid that is primarily made of red blood cells (RBCs), white blood cells, and platelets suspended in plasma. Under normal, healthy conditions, a freely suspended RBC is a biconcave discoid with 8-μm diameter and 2-μm thickness. RBCs constitute ~40–45% of the total blood volume. Being highly deformable particles, RBCs can easily squeeze through the smallest capillaries having internal diameter less than their characteristic size. The particulate nature of the blood and the deformability of the RBCs determine the overall rheological behavior of the blood.

In vitro studies on blood flow through narrow tubes have revealed complex rheological behavior of blood (1–6). In large vessels with internal diameter >500 μm, blood behaves as a Newtonian fluid with a constant viscosity. In vessels <500 μm, blood behaves as a non-Newtonian fluid. In such vessels, the viscosity of blood depends on the vessel diameter. This behavior is known as the Fahraeus-Lindqvist effect (7). It is characterized by a decrease in the apparent blood viscosity as the vessel diameter decreases below 500 μm. The minimum apparent viscosity is reached when the tube diameter is ~8 μm. Upon further decrease in tube diameter, the apparent viscosity increases very rapidly. The physical reason behind the Fahraeus-Lindqvist effect is the formation of a cell-free layer near the wall of the tube (8,9). The layer is devoid of RBCs and has a reduced local viscosity. The core of the tube, on the contrary, is rich with RBCs and has a higher local viscosity (10–13). The extent of the cell-free layer, which depends on the vessel size and hematocrit, is a major factor that determines the apparent viscosity of blood.

The formation of the cell free-layer is due to a migration of the red blood cells lateral to the mainstream flow and away from the wall of the vessel. The lateral migration arises due to the deformation of the red blood cells (14). As per the theory of viscous fluid mechanics (Stokes flow), a perfectly rigid particle does not migrate away from the wall, but a deformable particle does (15). The rate of migration depends on how easily the particle deforms; an easily deformable particle in a parabolic flow migrates faster toward the center of the vessel than a less deformable particle. The rate of migration also depends on the instantaneous radial location of the particle in the vessel. In a dilute suspension, individual RBCs continuously migrate toward the center of the vessel. In a dense suspension, hydrodynamic interaction between adjacent cells also affects their motion. The cell-free layer is formed under a balance between the deformation-induced lateral migration and the dispersion due to the cell-cell interaction (14).

Significant progress has been made in understanding the mechanical behavior of the red blood cells that have provided a basis for the study of cell deformation. Computational modeling and simulation of blood flow in microvessels have focused mainly on two issues: axisymmetric motion of a single cell in capillary tubes with diameter <10 μm (17–19), and the deformation of dilutely suspended cells in simple (linear) shear flows (20). Nonaxisymmetric motion of

Submitted August 9, 2006, and accepted for publication November 28, 2006.
Address reprint requests to Prosenjit Bagchi, E-mail: pbagchi@jove.rutgers.edu.

0006-3495/07/03/1858/20 $2.00
doi: 10.1529/biophysj.106.095042

RBCs in cylindrical capillaries has also been addressed (21). Development of more realistic simulation of multiple red blood cells flowing through vessels of diameter 10–500 μm has remained a major challenge. It is because blood in such vessels behaves as a multiphase suspension of deformable particles. While a continuum description of blood is sufficient for average flow profile, it is not so if the motion of individual cells and their interaction are concerned. The size of the RBCs is comparable to the size of the vessels, and hence each cell must be taken into consideration in the modeling. At the same time, multiple cells, often of the order of a few thousands in number, must be considered to realistically simulate a microvessel. Any computational model aimed at understanding blood flow in microvessels must take into consideration the deformability of the individual red blood cell, and an ensemble of a large population of cells.

A significant step in the simulations of flowing multiple RBCs has been achieved by Sun and Munn (22), who used a Lattice-Boltzmann simulation to address blood flow in 20–40 μm two-dimensional channels and at hematocrit of 10–30%. The simulations were two-dimensional, but the results showed that apparent viscosity of the suspension increases with increasing volume fraction of the particles, which is in agreement with the earlier observations with suspensions of RBC, and other rigid particles. However, the RBCs in their simulation were modeled as rigid disks, rather than deformable particles. Further, the range of channel size is not large enough to show the nonlinear behavior of the apparent viscosity with varying channel size. It should also be noted that at very high volume fractions, which were not considered by Sun and Munn, rigid particles can stop the flow. This is not the case with RBCs due to their flexibility.

In this article, we present computational simulation of the motion of red blood cells flowing through two-dimensional channels of size 20–300 μm. Similar to the work of Sun and Munn (22), we consider two-dimensional simulations. However, the deformability of the cells is included in our model. Moreover, a large cell population comprising of as high as 2500 red blood cells are simulated. To the best of our knowledge, this article presents the first simulation to consider such a large ensemble of deformable cells, though in two dimensions. As we will see later, many characteristics of the RBC motion, formation of the cell-free layer, and the Fahraeus-Lindqvist effect are quite accurately predicted by our two-dimensional simulations.

The structure of the article is as follows. In the next section, we describe the simulation technique, followed by presentation of the results. First, we describe the motion of an isolated red blood cell flowing through a vessel, and address its dynamic behavior, such as lateral migration, tank-treading, and flipping motion. We then consider simulations of multiple cells in the range of vessel size 20–300 μm and discharge hematocrit 10–60%. Number of RBCs considered in a typical simulation ranges from 5 to 2500. Results on the trajectory and velocity of individual cells and their fluctuation statistics are presented. The inclusion of deformability allows us to study the formation of the cell-free layer. Comparisons are made with the experimental results (1–4). We then present the apparent viscosity of blood for varying hematocrit and vessel diameter, and discuss the Fahraeus-Lindqvist effect. The numerical results also allow us to investigate variation of ''local'' apparent viscosity across the cross-section of the vessel.

SIMULATION TECHNIQUE

Flow configuration

The flow configuration is described in Fig. 1. The motion of an ensemble of red blood cells through a two-dimensional rectangular channel is considered. The undeformed resting shape of a red blood cell is taken to be a biconcave disk. In the figure, the flow is along the x direction and from left to right. The flow is driven by a constant pressure gradient. No-slip conditions are imposed at the walls of the channel. In absence of the cells, the velocity profile of the pure plasma is parabolic and is given by the Poiseuille law. The height of the channel is denoted by H, which is equivalent to the tube diameter in case of a three-dimensional flow. The computation domain is a square segment of sides of length H. Periodic conditions are imposed at the inflow (*left*) and outflow (*right*) of the domain. The cells that leave the domain through the outflow boundary are brought back into the domain through the inflow boundary.

Immersed boundary method

The simulation technique considered here is the immersed boundary method developed by Peskin (23), and later extended by Tryggvason and co-workers (24,25) as the front-tracking method for deformable interface. The method has been applied to the simulations of suspension of liquid drops and bubbles, and deformation of a red blood cell ghost in a shear flow (20). The method is particularly suitable for this study, as the red blood cells are modeled as liquid ''capsules.'' The structure of a red blood cell consists of hemoglobin solution surrounded by a lipid bilayer membrane. The liquidlike nature of hemoglobin, and the elastic nature of the membrane give rise to the deformability of the cell. On a mesoscopic scale, the detailed molecular structure of the lipid bilayer and the underlying two-dimensional cytoskeleton network can be neglected. Then, the individual RBC can be modeled as a liquid capsule, that is, a viscous liquid drop surrounded by a thin elastic membrane. The viscosity of the liquid interior (i.e., hemoglobin) of the capsule is five times higher than that of the exterior liquid (i.e., plasma).

In the present model, blood plasma and RBC hemoglobin are assumed to behave as Newtonian fluids. The Newtonian nature of these fluids is well established (26). The

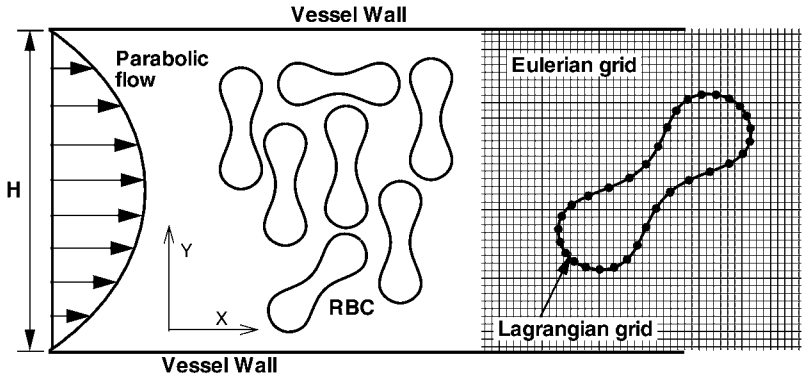

FIGURE 1 Schematic of the computational domain, and the Eulerian and Lagrangian grids.

non-Newtonian behavior of the whole blood primarily arises due to deformability of individual RBC. The motion of the liquids, plasma, and hemoglobin, is governed by the continuity and Navier-Stokes equations as

$$\nabla \cdot \mathbf{u} = 0, \tag{1}$$

$$\rho\left[\frac{\partial \mathbf{u}}{\partial t} + \mathbf{u} \cdot \nabla \mathbf{u}\right] = -\nabla p + \nabla \cdot \tau + \mathbf{F}, \tag{2}$$

where $\mathbf{u}(\mathbf{x}, t)$ is the fluid velocity, ρ is the density, p pressure, and $\mathbf{F}$ is a sourcelike term that arises due to the elastic force generated in the cell membrane. The viscous stress tensor τ is given by

$$\tau = \mu(\nabla \mathbf{u} + (\nabla \mathbf{u})^{\mathrm{T}}), \tag{3}$$

where $\mu(\mathbf{x})$ is the viscosity of either the plasma or the hemoglobin solution. For any point within the RBC, $\mu = \mu_{\mathrm{r}}$, and for any point outside the RBC, $\mu = \mu_{\mathrm{p}}$, where μ_{r} is the viscosity of the RBC hemoglobin, and μ_{p} is the viscosity of the plasma.

The main idea of the front-tracking method is to use a single set of equations for both fluids, plasma and hemoglobin, as in Eq. 2. The Navier-Stokes equations for the fluid flow are solved on a fixed Eulerian grid, and the cell-plasma interface is tracked in a Lagrangian manner by a set of moving grid, used to discretize the cell membrane as shown in Fig. 1. As the cells deform during their motion, the cell membranes are stretched, and elastic forces are generated on the membrane. The deformation of individual cell alters the surrounding flow. The elastic forces at the cell membranes are coupled to the bulk fluid motion via the source term $\mathbf{F}$ in Eq. 2 as

$$\mathbf{F}(\mathbf{x}, t) = \int_{\partial S} \mathbf{f}(\mathbf{x}', t)\delta(\mathbf{x} - \mathbf{x}')d\mathbf{x}', \tag{4}$$

where $\mathbf{f}(\mathbf{x}', t)$ is the elastic force generated in the membrane. Here $\mathbf{x}$ is the location of an arbitrary point in the flow domain, $\mathbf{x}'$ is any point on the membrane, and δ is the Delta function, which vanishes everywhere except at the membrane. Models for computation of $\mathbf{f}(\mathbf{x}', t)$ are described later.

The Navier-Stokes equations are first solved to obtain the fluid velocity and pressure. Then the cells are advected in a Lagrangian manner. The velocity of the cell membrane is obtained by interpolating the velocity of the fluid as

$$\mathbf{u}(\mathbf{x}') = \int_S \mathbf{u}(\mathbf{x})\delta(\mathbf{x} - \mathbf{x}')d\mathbf{x}, \tag{5}$$

where S denotes the entire flow domain. The membrane is then advected by

$$\frac{d\mathbf{x}'}{dt} = \mathbf{u}(\mathbf{x}'). \tag{6}$$

The δ-functions used in Eqs. 4 and 5 are constructed by multiplying one-dimensional delta functions, such as $\delta(\mathbf{x} - \mathbf{x}') = \delta(x - x')\delta(y - y')$, in two dimensions. For numerical implementation, a smooth representation of the δ-function is introduced as (24)

$$D(\mathbf{x} - \mathbf{x}') = \frac{1}{16\,\Delta^2}\prod_{i=1}^{2}\left(1 + \cos\frac{\pi}{2\Delta}(x_i - x_i')\right) \quad \text{for}$$
$$|x_i - x_i'| \le 2\Delta, \quad i = 1, 2$$
$$D(\mathbf{x} - \mathbf{x}') = 0 \quad \text{otherwise}, \tag{7}$$

where Δ is the Eulerian grid size. The above representation approaches the actual delta function as the grid size approaches zero. The discrete δ-function is so constructed that properties, such as viscosity, vary smoothly over four Eulerian grid points surrounding the RBC membrane. In discrete form, the integrals in Eqs. 4 and 5 can be written as

$$\mathbf{F}(\mathbf{x}_j) = \Sigma_i D(\mathbf{x}_j - \mathbf{x}_i')\mathbf{f}(\mathbf{x}_i'), \tag{8}$$

$$\mathbf{u}(\mathbf{x}'_i) = \Sigma_j D(\mathbf{x}_j - \mathbf{x}_i')\mathbf{u}(\mathbf{x}_j), \tag{9}$$

where i and j represent the Lagrangian and Eulerian grid points, respectively. The above representation needs to be modified if the interface is located close to a solid boundary. In our simulation, we ensure that the minimum distance between the solid boundary and the interface is at least four Eulerian grid size.

As the cells move to new positions, the viscosity $\mu(\mathbf{x}, t)$ needs to be updated. Following Tryggvason and Unverdi and Tryggvason (24,25), this is done by first defining an indicator function $I(\mathbf{x})$ such that

$$\mu(\mathbf{x}, t) = \mu_p + (\mu_r - \mu_p)I(\mathbf{x}, t). \tag{10}$$

To find the indicator function, we use a Poisson solver as

$$\nabla^2 I = \nabla \cdot \mathbf{G}, \tag{11}$$

where

$$\mathbf{G} = \Sigma_i D(\mathbf{x}_j - \mathbf{x}_i')\mathbf{n}\Delta s, \tag{12}$$

and where D is the discrete δ-function as given in Eq. 7, $\mathbf{n}$ is the unit normal to the cell surface, and Δs is a discrete line segment on the cell surface. In this way, the direct solution of the advection equation for viscosity, and hence the smearing of viscosity profile across the interface are avoided. Here we avoid the details of the method, and refer to articles by Tryggvason and co-workers (24,25).

RBC model

As mentioned before, red blood cells in this study are modeled as liquid "capsules," that is, viscous liquid drops surrounded by elastic membranes. The viscosity of the liquid interior (i.e., hemoglobin) of the capsule is five times higher than that of the exterior liquid (i.e., plasma). This difference is taken into account in the immersed boundary method described above. The deformation of the cells under a dynamic fluid motion generates an elastic force $\mathbf{f}(\mathbf{x}', t)$ in the cell membrane. Computation of this force requires a constitutive law for the material of the membrane. Here we assume that the membrane follows the neo-Hookean law. Note that the neo-Hookean law does not strictly represent the behavior of a red blood cell membrane. An RBC membrane is strongly resistant to area dilatation. On the contrary, the neo-Hookean model employed here does allow area dilatation. Membrane models that restrict area dilatation and hence are more accurate for the RBC have been developed (27,28). The present methodology does allow incorporation of these models. The neo-Hookean model is chosen because of its simplicity. An accurate modeling of cell deformation is not the goal of this article. For the present purpose, a cell model that takes into account deformability is sufficient. Indeed, it is shown later that the neo-Hookean model can effectively capture some general characteristics of the RBC motion in a shear flow, such as the tank-treading motion and the lateral migration.

For a two-dimensional neo-Hookean membrane of a three-dimensional cell, the strain energy function is given by (20)

$$W = E_s h(\epsilon_1^2 + \epsilon_2^2 + \epsilon_1^{-2}\epsilon_2^{-2}), \tag{13}$$

where E_s is the shear modulus of elasticity of the membrane, h is the thickness, and ϵ_1 and ϵ_2 are the principal stretch ratios. The tensions T_1 and T_2 in the principal directions are then given by (29)

$$T_1 = \frac{E_s h}{\epsilon_1\epsilon_2}\left(\epsilon_1^2 - \frac{1}{(\epsilon_1\epsilon_2)^2}\right) \quad \text{and} \quad T_2 = \frac{E_s h}{\epsilon_1\epsilon_2}\left(\epsilon_2^2 - \frac{1}{(\epsilon_1\epsilon_2)^2}\right). \tag{14}$$

For the two-dimensional simulations considered here, the membrane is a closed curve. A two-dimensional cell is then equivalent to an actual three-dimensional cell subject to a stretching in one direction only. That is, $T_1 \neq 0$, $T_2 = 0$, where *1* indicates the in-plane direction along the membrane, and *2* indicates the out-of-plane direction normal to Fig. 1. The deformation ϵ_2 in the out-of-plane direction is not zero. But since $T_2 = 0$, we can express ϵ_2 in terms of ϵ_1. Then, for a two-dimensional cell, we have

$$T = \frac{E_s h}{\epsilon^{3/2}}(\epsilon^3 - 1), \tag{15}$$

where $T = T_1$ and $\epsilon = \epsilon_1$. For a discretized cell, T is the tension acting along a line segment connecting two adjacent Lagrangian grid points on the membrane, and ϵ is the stretch ratio (undeformed length by deformed length) of the line segment. At any Lagrangian grid point on the membrane, two line segments meet. The membrane elastic force $\mathbf{f}$ is then the resultant vector of the tensions in the two adjacent segments,

$$\mathbf{f} = T_i\mathbf{e}_i - T_j\mathbf{e}_j, \tag{16}$$

where i and j denotes two adjacent line segments, and $\mathbf{e}_i$ and $\mathbf{e}_j$ are the unit tangent vectors along them.

The RBC membrane also has a bending resistance. To include the bending resistance in our simulation, we follow the approach by Pozrikidis (30). Equation 16 is then modified as

$$\mathbf{f} = T_i\mathbf{e}_i - T_j\mathbf{e}_j + q\mathbf{n}, \tag{17}$$

where $q = dm/dl$ is the transverse shear tension, $m = E_B(\kappa - \kappa_r)$ is the bending moment, E_B is the bending modulus, κ is the local curvature, κ_r is the reference curvature in resting configuration, l is the arc length along the membrane, and $\mathbf{n}$ is the unit normal vector at a Lagrangian marker point on the cell surface.

Dimensionless parameters, finite difference scheme, and resolution

In absence of the cells, the maximum velocity of the parabolic flow at the channel center is denoted by U_{cl}. The governing equations are made dimensionless using the channel height H as the characteristic length scale, U_{cl} as the velocity scale, and H/U_{cl} as the timescale. In dimensionless form, the shear modulus of elasticity of the RBC membrane is given by $E^* = \mu_p U_{cl}/E_s h$, which is the ratio of the viscous force to the elastic force of the capsule membrane. The dimensionless bending stiffness is expressed as $E_B^* = E_B/(a^2 E_s)$,

where a is a characteristic dimension of the cell. The Reynolds number of individual RBC, defined as $Re = \rho U_{cl} a/\mu_p$, is much less than unity.

In the present model, the dimensionless parameters E^* and E_B^* determine the deformability of the liquid capsule, and hence of the red blood cell. For a normal, healthy red blood cell, $E_s = 0.006$ dyn/cm, and $E_B \approx 1.8 \times 10^{-12}$ dyn-cm (6). Under diseased conditions, e.g., in sickle cell anemia, the cells lose their deformability. The loss of deformability can be expressed in our model in terms of higher-than-normal values of E_s and E_B. Accordingly, the values of E^* and E_B^* change as the cell loses its deformability. The value of E^* also depends on the flow velocity U_{cl}. Note that in presence of the RBCs, the maximum centerline velocity is significantly reduced below U_{cl} if the pressure gradient is kept constant (shown later in Plug-Flow Profile). The average flow velocity in presence of the RBCs is denoted by U_m. In our simulations, U_m ranges from ~3 mm/s to 15 mm/s (Table 2). Accordingly, the values of E^* and E_B^* used in our simulations ranges from ~0.02–1.0, and 0.0005–0.002, respectively. The higher values of E^* and lower values of E_B^* typically represent a normal, deformable RBC, whereas lower values of E^* and higher values of E_B^* represent a less deformable RBC. The higher values of E^* also represent higher flow velocities, and vice versa. The range of U_m considered here matches with that in the in vivo experiments (1,2). A pseudo-shear rate can also be defined as U_m/H, which varies between ~30 and 400 s^{-1}, similar to the range in Bishop et al. (1,2). In terms of physical time, the simulations represent 0.1 s of flow, on the average.

The governing equations are discretized spatially using a finite difference scheme, and temporally using a two-step time-split scheme. In this method, the momentum equation is split into an advection-diffusion equation and a Poisson equation for the pressure. The body-force term is retained in the advection-diffusion equation. The nonlinear term in this equation is treated explicitly using a second-order Adams-Bashforth scheme. To avoid a stability problem, we treat the viscous terms implicitly using an alternating-direction implicit scheme. In the method, three one-dimensional implicit equations are obtained, which are solved directly by a tridiagonal matrix solver. The velocity is not divergence-free at the end of the advection-diffusion step. The Poisson equation is then solved to obtain pressure at the next time level. Using the new pressure, the velocity field is corrected to make it divergence-free. To reduce expensive computation, the Poisson equation is Fourier-transformed in the periodic direction yielding a set of one-dimensional decoupled PDEs, which is directly inverted to obtain pressure. Details of the time-step scheme are given in Bagchi and Balachandar (31).

The accuracy of the simulations depends on the resolution of the Eulerian and Lagrangian grids. A detail study of the resolution and validation of the computational model are given elsewhere and not repeated here (32). In deciding the resolution, we make sure that there is a sufficient number of Eulerian points within each cell area, and in the region between two adjacent cells. Typically, for a circular cell, ~25 Eulerian points per diameter are found to be sufficient (33).

The resolution used in the present simulations is given in Table 1. It varies from 129 × 128 Eulerian grids for a 20-μm channel to 2049 × 2048 grids for a 300-μm channel. The Lagrangian resolution varies from 128 to 512 marker points per cell. The Lagrangian resolution is increased as the cell deformability increases to ensure that strong curvatures in the cell shape are well resolved. The requirement for a high Eulerian resolution renders some of our computations very expensive, even in two dimensions. Efficient algorithm based on fast Fourier transform, and OpenMP parallelization, have been implemented to speed up the computation. The simulation for a 80-μm channel with 501 × 500 Eulerian resolution takes ~50 CPU hours on 1.6 GHz IBM p690 processors for 50,000 timesteps.

A typical dimensionless time-step size used is ~0.001. In the present method, the immersed boundaries are advected explicitly. In many cases, however, the explicit treatment of the immersed boundary results in more restrictive stability conditions than the viscous terms of the Navier-Stokes equations. For the present simulations, this is not the case due to the specific constitutive law used.

RESULTS

Motion of an isolated RBC

First we describe the motion of a single, isolated RBC in a parabolic flow in a rectangular channel of $H = 40$ μm. The results are shown in Figs. 2 and 3. The initial resting shape of the cell is biconcave. At time $t = 0$, the cell is located close to the wall of the channel. As the flow starts, the cell deforms

TABLE 1 Channel size, discharge, and tube hematocrits, and Eulerian grid resolutions used in the present simulation

Channel size (H, μm)	H_d %	H_t %	Number of RBC	Eulerian resolution
20	20	12	3	129 × 128
20	30	20	5	129 × 128
20	45	33	7	129 × 128
20	60	48	10	129 × 128
40	10	6.4	5	249 × 248
40	20	13.5	11	249 × 248
40	45	35	28	249 × 248
40	60	50	40	249 × 248
80	10	7.6	32	501 × 500
80	20	15.7	66	501 × 500
80	45	38	160	501 × 500
80	60	54	227	501 × 500
150	20	18	251	1025 × 1024
150	45	43	600	1025 × 1024
150	60	57	800	1025 × 1024
300	45	44	2500	2049 × 2048

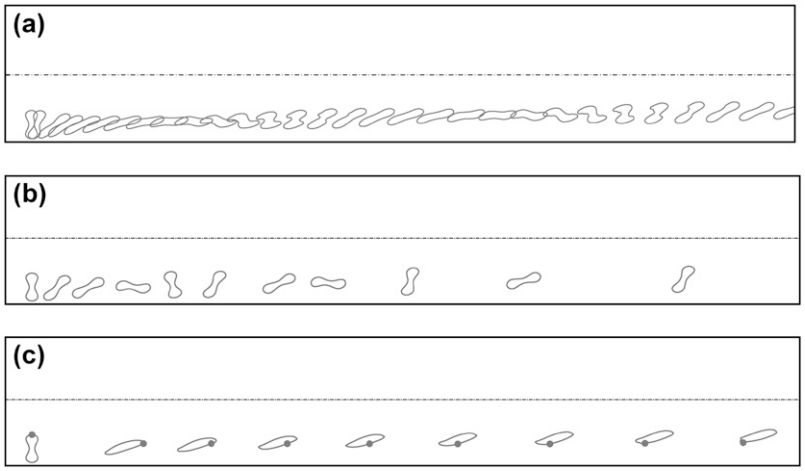

FIGURE 2 Motion of an isolated RBC in parabolic flow through a 40-μm channel. The flow is from left to right and the center of the channel is shown by (- · - · - · -). (*a*) Normal, deformable RBC; (*b*) less deformable RBC; and (*c*) RBC with reduced membrane resistance. A point on the cell surface is shown to illustrate the tank-treading motion.

and moves longitudinally along the flow direction as well as laterally normal to the flow. Three cases are simulated to study the role of cell deformability: case *a*, a normal RBC at $E^* = 0.2$ and $E_B^* = 0.0005$; case *b*, a less deformable RBC with $E^* = 0.02$ and $E_B^* = 0.002$; and case *c*, a RBC with reduced membrane resistance ($E^* = 1.0$, $E_B^* = 0.0005$).

As shown in Fig. 2, the RBC in cases *a* and *b* undergoes significant deformation during its motion in the parabolic flow through the channel. A normal cell, as in case *a*, repeatedly attains biconcave shape and elliptic shape. The biconcave shape is attained when the major axis of the cell is aligned nearly normal to the flow direction. The elliptic shape is attained when the major axis is between 0° and 45° with the flow direction. At reduced membrane resistance, as in case *c*, the biconcave shape is completely lost, and the cell attains a nearly elliptic shape. For the less deformable cell, as in case *b*, no significant deformation is observed, and the cell maintains the biconcave shape throughout its motion.

For an RBC placed in a shear flow, two modes of motion have been observed by previous researchers, both experimentally and computationally: tank-treading motion and tumbling motion (14,18,34,35). In the tank-treading mode, the cell membrane and the interior liquid undergo steady rotary motion while the cell maintains a fixed orientation with the flow. In the tumbling motion, the cell flips like a rigid body. The transition from tank-treading to tumbling motion occurs as the deformability of cell decreases. Our results in Fig. 2 reproduce these earlier observations. For the RBC with reduced membrane resistance, as in case *c*, only tank-treading motion is observed. In the figure, an arbitrary point on the cell surface is marked to show the tank-treading motion. For the less deformable RBC, as in case *b*, only tumbling motion is observed. On the contrary, for the normal RBC, as shown in case *a*, simultaneous tumbling and tank-treading motions are observed. The frequency of tumbling motion increases as the deformability decreases.

For all cases considered, the RBC is observed to migrate laterally away from the wall toward the center of the channel under the action of the parabolic flow. The lateral position of the center of the RBC is shown in Fig. 3 *a*. In general, the migration is a very slow process; for the normal RBC, the cell travels only 10 μm in the lateral direction while moving nearly 2500 μm in the longitudinal direction. The rate of migration depends on the deformability of the cell. Rate of

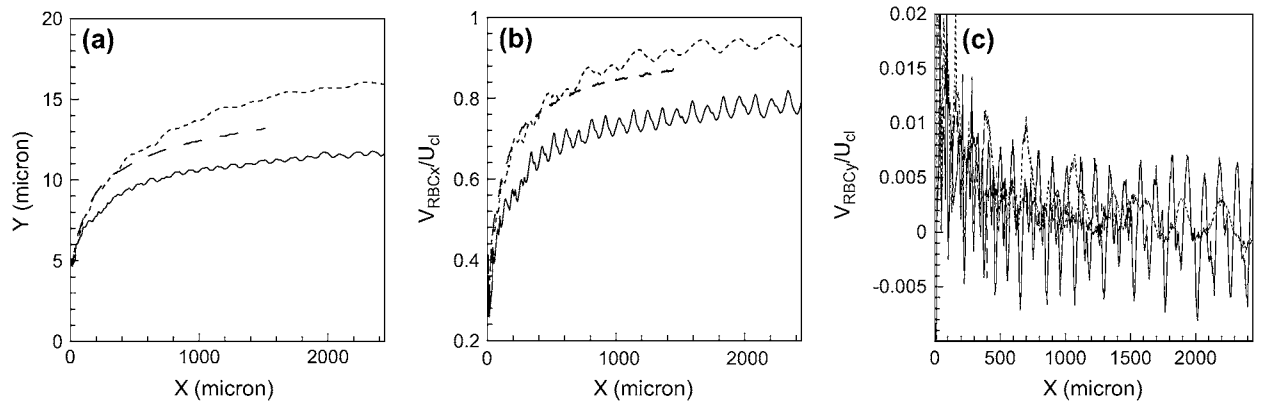

FIGURE 3 (*a*) The *x*-*y* trajectory, (*b*) longitudinal velocity, and (*c*) lateral velocity of the cells shown in Fig. 2. (··· ···) Normal cell (case *a* in Fig. 2); (——) less deformable cell (case *b*); (- - - -) cells with reduced membrane resistance (case *c*).

migration is lower for the less deformable RBC as in case *b* than in cases *a* and *c* in Fig. 2. Interestingly, we also observe that the migration rate is higher for the normal cell, as in case *a*, than that for a cell with reduced membrane resistance, as in case *c*. Note that the normal RBC in case *a* performs both deformation and tumbling motion. On the contrary, no tumbling motion is seen in case *c*. The results suggest a possible coupling between deformation and the tumbling motion, which results in a higher migration rate in case *a*.

The longitudinal and the lateral velocity components of the RBC are shown in Fig. 3, *b* and *c*. Clearly, the lateral component is an order-of-magnitude less than the longitudinal component. The velocity components, as well as the lateral position, show fluctuations for the normal cell and the less deformable cell. These fluctuations arise due to the tumbling motion. The lateral velocity may become periodically negative due to the tumbling motion as in the case of the less deformable cell. Within one cycle of oscillation, the migration velocity becomes maximum when the cell is aligned nearly at 45° with the flow, and minimum at 135°. Oscillation increases with decreasing deformability.

The above results represent the dynamics of a red blood cell in a dilute suspension flowing through a conduit. The results presented here on the lateral migration of the RBC agree with the glass tube experiments (14). Clearly, the present computational model is able to capture the general dynamic behavior of a red blood cell in a parabolic flow, particularly the tank-treading and tumbling motion, and the lateral migration. As mentioned before, the lateral migration leads to the formation of the cell-free layer, which serves as the primary mechanism for the Fahraeus-Lindqvist effect. In a nondilute suspension, the presence of many RBCs affects the motion of individual cell, and the formation of the cell-free layer. It is of interest in the next section to study how the motion of individual cell is affected in presence of neighboring cells.

It should be noted that according to Keller and Skalak (35), an ellipsoid with an internal-to-external viscosity ratio of 5 would tumble rather than rotate even at high shear rate. The results in Fig. 2 *c* may appear to be in contrast to their result. In Keller and Skalak (35), the particles are nondeformable. For a deformable cell, the transition from flipping to tank-treading motion also depends on the aspect ratio of the cell, and hence the extensional resistance of the membrane. Note that the neo-Hookean model used here for the cell membrane does allow continuous extension of the membrane with increasing shear rate. Ramanujan and Pozrikidis (36) considered the large-deformation of ellipsoidal and biconcave capsule in shear flow using neo-Hookean model, and showed that at viscosity ratio of 5, an ellipsoidal cell performs only oscillatory motion rather than a flipping motion. Their result indicates that the ellipsoid is eventually likely to achieve a steady orientation. The biconcave discoid however showed a flipping motion. If the initial shape is spherical, the deformed ellipsoidal cell does not show even an oscillatory motion at viscosity ratio 5.

As far as the deformation of a cell is concerned, the viscosity ratio and the elastic resistance of the cell membrane contribute in the same way. That is, an increase in any of these two parameters would cause less deformation. Since high viscosity ratio causes transition from tank-treading to flipping motion, so likely does the higher membrane resistance. Thus allowing the membrane deformability, which is neglected in Keller and Skalak (35), may delay the transition from tank-treading to flipping motion only to a viscosity ratio >5. In fact, if membrane deformability is allowed, as done in our article, the cell would elongate more at a given viscosity ratio. Keller and Skalak (35) mentioned that increasing the elongation promotes a stationary orientation of the cell. Thus, the result in Fig. 2 *c* is not completely in opposite to that of Keller and Skalak (35).

Motion of RBC suspension

We now present the results on the simulation of suspension of multiple red blood cells. As mentioned before, the size of the vessel ranges from $H = 20$–300 μm, and the discharge hematocrit $H_d = 10$–60%. The number of red blood cells considered in our simulations varies from 5 to 2500. Note that in the simulations, discharge hematocrit is not directly specified. Instead, we specify the tube hematocrit H_t that varies from 6 to 57%. In Table 1, we have listed the discharge hematocrit, corresponding tube hematocrit, and the number of RBCs in various numerical experiments considered here. In the subsequent results, both tube and discharge hematocrits are mentioned. For a given discharge hematocrit, the tube hematocrit is first obtained as (3)

$$\frac{H_t}{H_d} = H_d + (1 - H_d)[1 + 1.7\,e^{-0.35D} - 0.6\,e^{-0.01D}], \quad (18)$$

where $D \equiv H$ is the tube diameter. Once the tube hematocrit is obtained, the number of red blood cells within the computation domain is found by knowing the cell volume (or, area, in two dimensions). The computation domain is a square segment of the channel. The initial shape of the cells is biconcave, and the cells are initially distributed in a random manner throughout the domain. The flow starts at time $t = 0$ under a constant pressure gradient. In the simulations, the velocity and pressure fields of the fluid, and the coordinates, shapes, and velocity of the cells are stored at frequent time intervals. Instantaneous distributions of the red blood cells in the vessels are shown in Figs. 4–7 for a few representative cases. Simulations are performed over sufficient time so that quasi-steady state is reached.

Shown in Fig. 4 are the results for a 20-μm channel. Three different cases are considered here: suspension of 1), normal RBCs at $H_t = 20\%$ ($H_d = 30\%$); 2), normal RBCs at $H_t = 48\%$ ($H_d = 60\%$); and 3, less deformable RBCs at $H_t = 20\%$ ($H_d = 30\%$). Time evolution of the cell distribution is shown in the figure, and a few cells are marked by numbers.

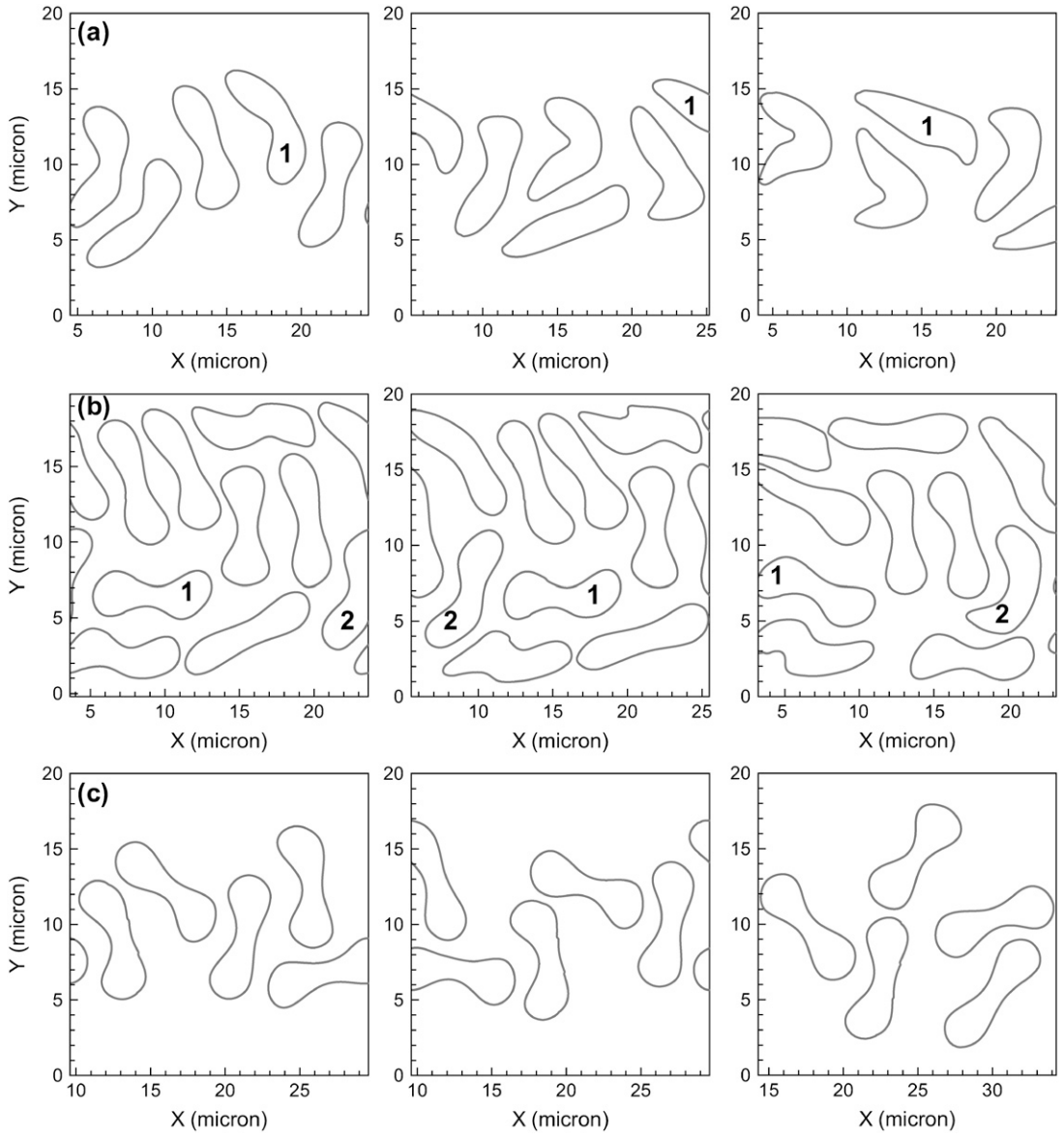

FIGURE 4 RBC suspension in a 20-μm channel. (*a*) Normal RBC at $H_t = 20\%$ ($H_d = 30\%$); (*b*) normal RBC at $H_t = 48\%$ ($H_d = 60\%$); and (*c*) less deformable RBCs at $H_t = 20\%$ ($H_d = 30\%$). For each case, three time instances are shown. The mean velocities are (*a*) 7.5 mm/s; (*b*) 3.5 mm/s; and (*c*) 4.7 mm/s. The third plots for panels *a*–*c* represent ~500 ms after the onset of flow.

First consider case *a*, for normal RBCs at $H_t = 20\%$. As the flow develops, the cells migrate toward the center of the channel, and the regions near the walls become devoid of RBCs. However, continuous lateral migration is prevented due to the presence of the neighboring cells. A balance between the hydrodynamic interactions among the cells and lateral migration of individual cell is attained, and a cell-free layer near the wall develops. Significant deformation of the RBCs is observed. Nearly all cells lose their biconcave shape. Unlike the case of a single, isolated RBC as considered in the previous section, none of the cells in suspension performs tumbling motion. The repeated emergence of the biconcave and elliptic shapes as observed before are also not seen here. However, the shapes are changing continuously due to the interaction with the neighboring cells. The RBCs near the center assume slipper shapes, whereas those further away from the center assume nearly elliptic shapes. The slipper shapes of the RBCs in vessels of this range of size have been observed in experiments and previous numerical simulations (6,37).

When the tube hematocrit is increased to $H_t = 48\%$ ($H_d = 60\%$), the cells are more evenly distributed across the channel. The cell-free layer is not well developed. The continuously changing shapes of the cells are still observed, although the slipper shape near the center is less common now. For less deformable RBCs at $H_t = 20\%$, as in case *c*,

the initial biconcave shape of individual cell is retained through the simulation. The tumbling motion of the cells is evident here. Tumbling motion results in a higher dispersion of the cells. As a result, the cell-free layer near the wall is reduced compared to that for the normal RBCs at the same H_d. The interface between the cell-free and cell-rich regions is also not well defined due to the cell-cell interaction.

The results for normal RBCs in 80- and 150-μm channels are shown in Fig. 5, while those in 300-μm channel are shown in Fig. 6. In these figures, discharge hematocrit is kept constant at $H_d = 45\%$. The tube hematocrits are 38%, 43%, and 44%, respectively. As the vessel size increases, the slipper shape of individual RBC is no longer observed. However, deformation of red blood cells is evident in all cases. The figures show that the cells near the wall deform

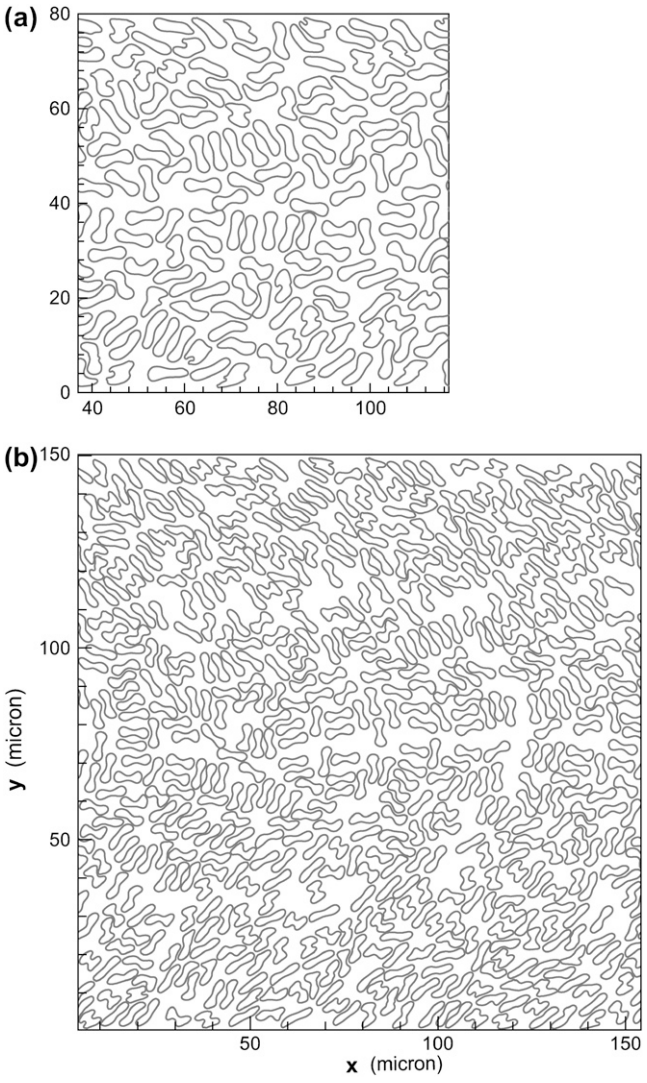

FIGURE 5 Suspension of normal RBCs at $H_d = 45\%$ in (*a*) 80-μm channel, and in (*b*) 150-μm channel. The tube hematocrits are 38% and 43%, respectively. The computation domain contains 160 cells in panel *a* and 600 cells in panel *b*. Mean velocities are (*a*) 5 mm/s, (*b*) 6.5 mm/s. The figures represent ~300 ms after the onset of flow.

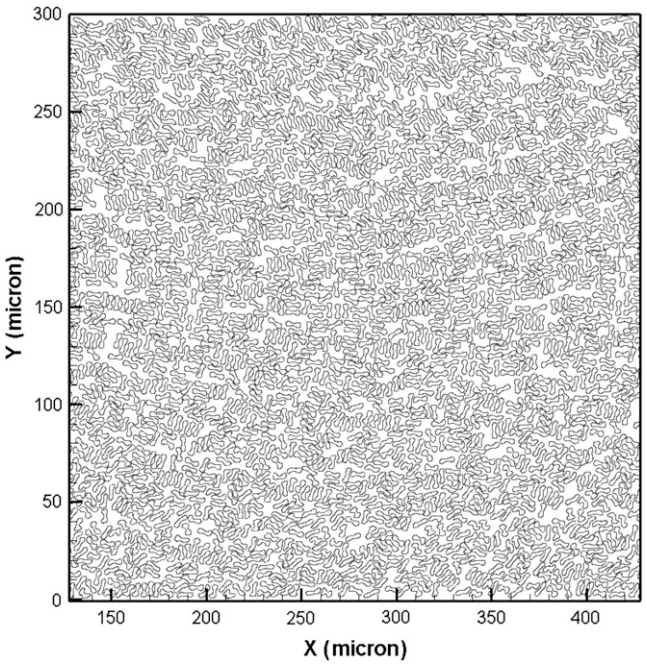

FIGURE 6 Suspension of normal RBCs in 300-μm channel at $H_d = 45\%$ ($H_t = 44\%$). A total of 2500 cells are simulated in the computation domain as shown above. Mean velocity is 12 mm/s. The figure represents ~150 ms after the onset of flow.

more and lose their biconcave shape, whereas the cells near the center deform less and retain the biconcave shape. This behavior is expected, since the fluid shear rate decreases from the wall toward the center. Tumbling motion of the cells appears to be suppressed. Most cells near the wall are aligned at an angle with the flow direction, whereas the cells near the center are nearly vertical or parallel to the flow.

The results for less deformable cells are shown in Fig. 7 for 80- and 150-μm channels. As expected, less deformable cells retain their biconcave shape, and perform the tumbling motion. The tumbling motion is stronger for the cells located near the wall than those located near the center. This observation is consistent with the hydrodynamic theory of particle motion in shear flow. The rate of tumbling is proportional to the shear rate of the fluid, which decreases from the wall toward the center of the vessel. However, due to higher hematocrit, tumbling motion is not as strong as that of an isolated RBC as was observed in Fig. 2 *b*. In general, the direction of the tumbling motion of individual cells in suspension matches with that of an isolated cell. In the lower half of the vessel, the cells tumble in the clockwise direction, whereas in the upper half they tumble counterclockwise, in accordance with the direction of vorticity of the flow. However, in some cases, strong cell-cell interaction is observed to reverse the direction of rotation. The tumbling motion combined with the cell-cell interaction results in random orientation of the cells across the channel.

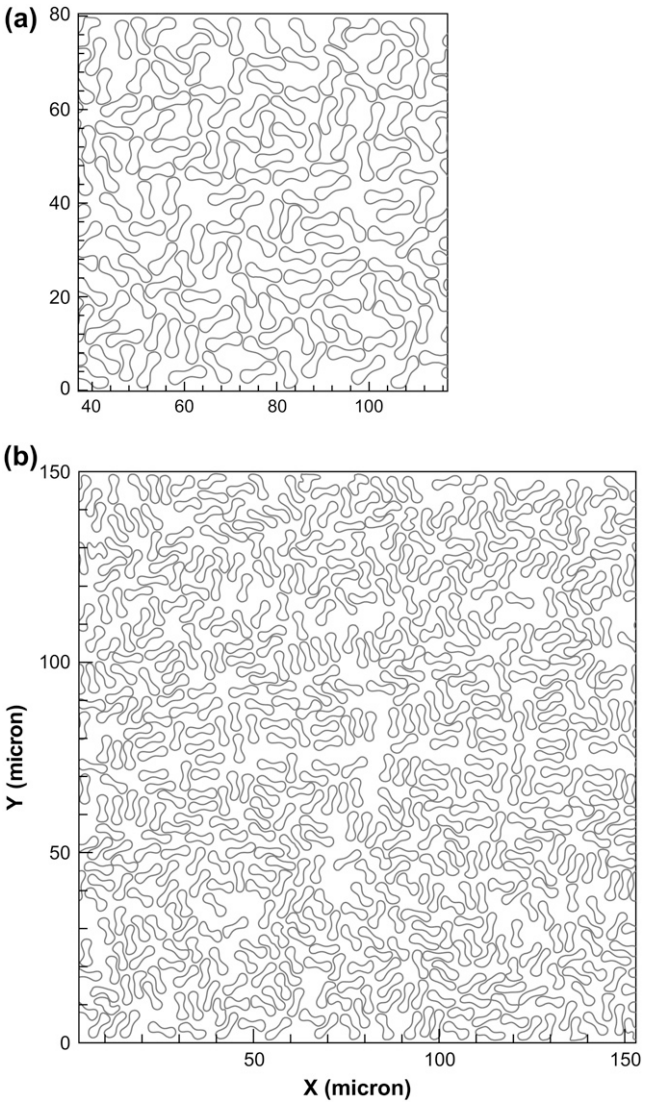

FIGURE 7 Suspension of less deformable RBCs at $H_d = 45\%$ in (*a*) 80-μm channel and (*b*) 150-μm channel. The tube hematocrits are 38% and 43%, respectively. The computation domain contains 160 cells in panel *a* and 600 cells in panel *b*. Mean velocities are (*a*) 3.6 mm/s and (*b*) 4.9 mm/s. The figures represent 300 ms after the onset of flow.

It should be noted that in experiments with flowing RBC suspension, the biconcave shape is usually not observed. In the present simulations, we have considered both normal and hardened cells. The hardened cells, as considered in Fig. 7, are expected to retain the biconcave shape due to the high bending-resistance values used to model them. The normal cell, after sufficient simulation time, would lose its biconcave shape. This is evident in Fig. 4, *a* and *b*. In Fig. 5, most cells near the channel wall lose the biconcave shape due to local high shear rate. However, these cells are tumbling also. So their shape repeats between biconcave and elliptic shapes, as it was observed for an isolated cell in Fig. 2 *a*. As for Fig. 6, the simulation is performed for a short time, since this case is computationally expensive. The two-dimensionality of the problem can also affect the cell shape as a real three-dimensional cell would deform more easily and may lose the biconcave shape on a shorter timescale than a two-dimensional cell.

RBC trajectory and velocity traces

In our simulations, the position and velocity of all red blood cells are tracked in time. These data allow us to study the trajectory and instantaneous velocity of individual red blood cell in the suspension. The trajectory of a few cells are shown in Figs. 8 and 9, and the velocity traces are shown in Fig. 10. The cells were tracked over a longitudinal distance that ranges from 500 to 2000 μm, depending on the specific simulation. As evident in the figures, individual red blood cells exhibit fluctuations in lateral position and velocity. Fluctuations arise due to the tumbling motion of individual cells as well as from interaction with neighboring cells.

First consider a 40-μm channel with normal RBCs, for which three different hematocrits are considered in Fig. 8: case *a*, $H_d = 10\%$; case *b*, $H_d = 20\%$; and case *c*, $H_d = 60\%$. The corresponding tube hematocrits are 6.4, 13.5, and 50%. In case *a*, lateral migration of the red blood cells initially located close to the wall is observed. However, the rate of migration of a cell in the suspension is much lower than that of an isolated RBC possibly due to cell-cell interaction. Moreover, unlike an isolated cell, the cells in suspension do not migrate continuously. Rather, the trajectories show random fluctuations due to the cell-cell interaction. A comparison of the three cases shows that the fluctuations in the RBC trajectory depend on the hematocrit. For case *a* at $H_d = 10\%$, oscillations in the trajectory are similar to those observed previously in Motion of an Isolated RBC for an isolated red blood cell. Such small-amplitude, low-frequency fluctuations are due to the tumbling motion of individual cells. The cell-cell interaction is less in this case of low H_d. As H_d increases to 20%, as in case *b*, the trajectory becomes more erratic. Large amplitude but less frequent fluctuations are observed which are due to the increased interaction between the cells. Upon further increase of H_d to 60%, small amplitude frequent fluctuations are nearly suppressed. At this higher hematocrit, the cells move in a nearly stacklike manner. The tumbling motion of individual cells is nearly inhibited, and the fluctuations result mostly from the cell-cell interaction.

The effect of increasing channel size is shown in Fig. 9 *d* where the 150-μm channel at $H_d = 20\%$ ($H_t = 18\%$) is considered. Note that for this vessel, only half of the cross section is shown. A slow migration of the cells away from the wall is observed. Fluctuations in the lateral position of the cells indicative of the tumbling motion of individual RBC and cell-cell interactions are observed. In Fig. 9 *a* we show the effect of increasing hematocrit while channel size is kept constant at 150 μm. The fluctuations in the lateral position

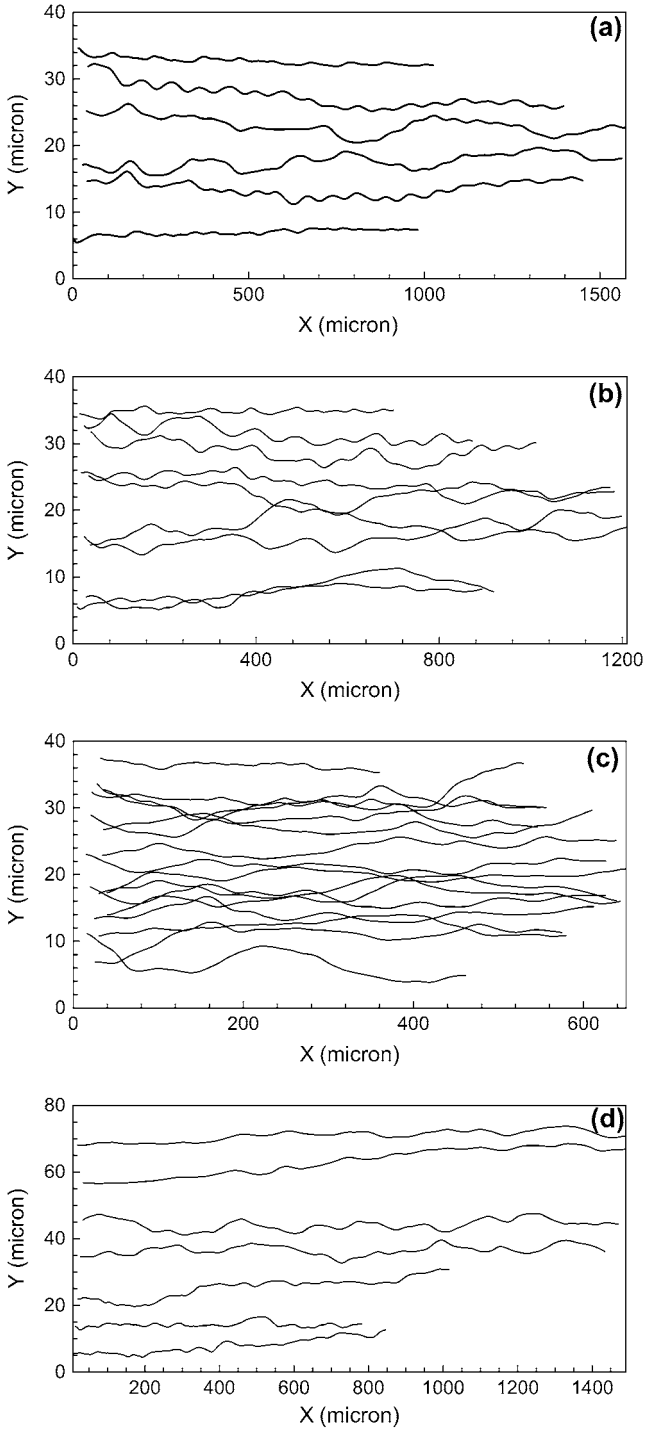

FIGURE 8 Trajectory of normal red blood cells in suspension flowing through a vessel. Panels *a–c* represent a 40-μm channel at $H_d = 10$, 20, and 60%, respectively. Corresponding tube hematocrits are 6.4, 13.5, and 50%. (*d*) 150-μm channel at $H_d = 20\%$ ($H_t = 18\%$). For panel *d*, only half of the channel is shown.

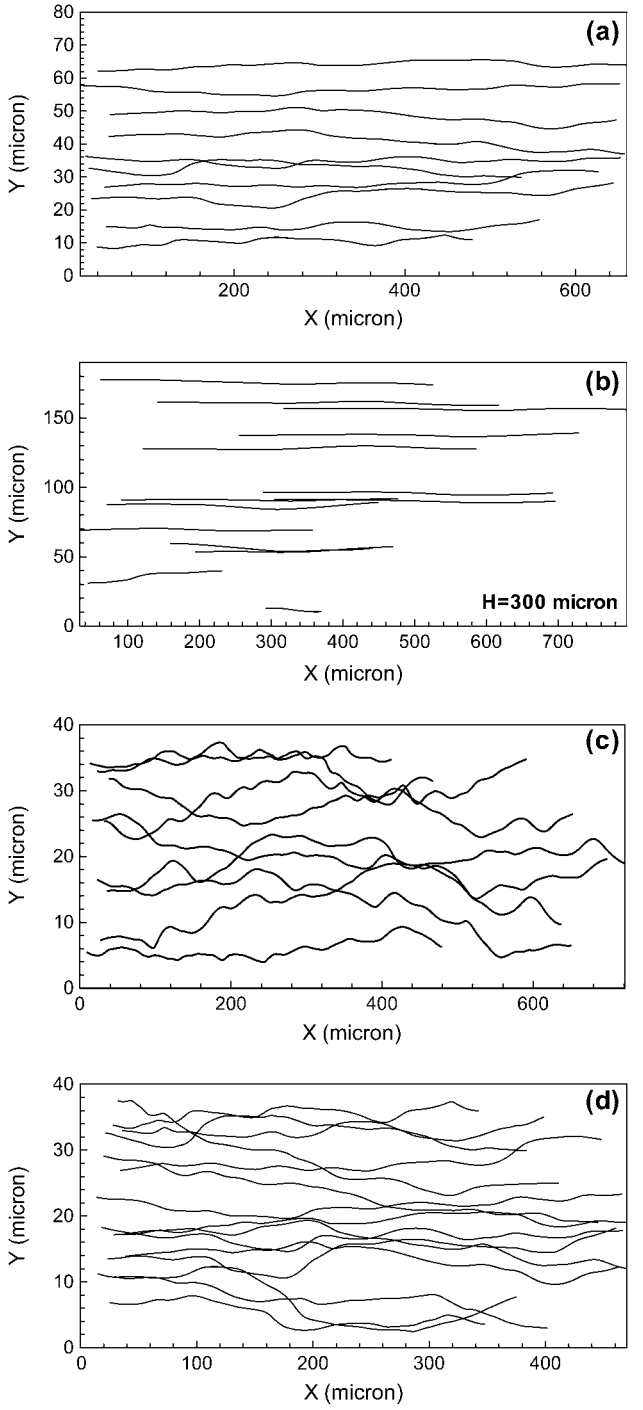

FIGURE 9 Trajectory of red blood cells in suspension flowing through a vessel. (*a*) Normal cells in a 150-μm channel at $H_d = 45\%$ ($H_t = 43\%$); (*b*) normal cells in a 300-μm channel $H_d = 45\%$ ($H_t = 44\%$); (*c*) less deformable cells in a 40-μm channel at $H_d = 20\%$ ($H_t = 13.5\%$); and (*d*) fewer deformable cells in a 40-μm channel at $H_d = 60\%$ ($H_t = 50\%$). In panels *a* and *b*, only half of the channel is shown.

appear to diminish at $H_d = 45\%$ ($H_t = 43\%$). Finally, for the 300-μm channels as shown in Fig. 9 *b* for $H_d = 45\%$ ($H_t = 44\%$), fluctuations in the trajectory are significantly reduced, and the cells appear to move in a stacklike manner.

The results for less deformable RBCs in a 40-μm channel are shown in Fig. 9, *c* and *d*, for $H_d = 20$ and 60%, respectively. The tube hematocrits are 13.5 and 50%, respectively. The trajectory at 20% hematocrit now shows more

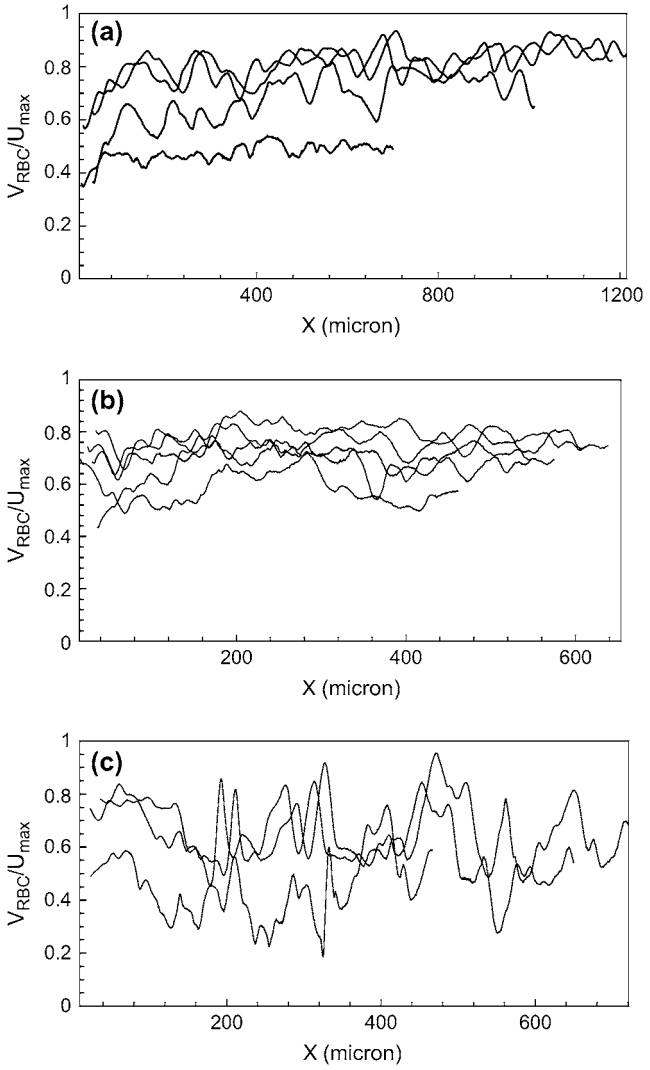

FIGURE 10 Velocity traces of red blood cells in suspension flowing through a 40-μm channel. (*a*) Normal cells at $H_d = 20\%$ ($H_t = 13.5\%$); (*b*) normal cells at $H_d = 60\%$ ($H_t = 50\%$); and (*c*) less deformable cells at $H_d = 20\%$ ($H_t = 13.5\%$). Mean velocity of whole blood for various cases can be found from Table 2. The velocity of RBCs is scaled with the centerline velocity.

erratic behavior compared to those for the normal RBCs. This behavior can be explained based on the results presented in the previous sections. A less deformable cell performs a strong tumbling motion, which can significantly affect the motion of the neighboring cells, resulting in more chaotic trajectory. Interestingly, some cells are seen to move toward the wall of the vessel, rather than the center. This anomalous behavior is due to the dispersion of the RBCs resulting from a strong cell-cell interaction. At higher hematocrit, as shown in Fig. 9 *d*, the tumbling motion is again inhibited, and the cells appear to move in nearly straight lines as in the case of normal RBCs.

The velocity traces of the RBCs in a 40-μm channel are shown in Fig. 10 for three cases: case *a*, normal RBCs at $H_d = 20\%$ ($H_t = 13.5\%$); case *b*, normal RBCs at $H_d = 60\%$ ($H_t = 50\%$); and case *c*, less deformable RBCs at $H_d = 20\%$ ($H_t = 13.5\%$). In the figure, cells with higher velocity are flowing closer to the center. Oscillations in the velocity traces are larger than those observed earlier for isolated red blood cell. The increased oscillation is due to the cell-cell interaction in the suspension. The oscillations significantly increase as the cells lose deformability, implying increased dispersion due to cell-cell interaction.

Statistics on RBC motion

Root mean-square (RMS) of the fluctuations in the lateral position, and the coefficient of variation (CV) of velocity can be obtained for each red blood cell in the simulations. These quantities are defined as

$$RMS = \left[\int_0^t (y(t) - \bar{y})^2 \, dt/T\right]^{1/2}, \tag{19}$$

and

$$CV = \frac{\left[\int_0^t (v(t) - \bar{v})^2 \, dt/T\right]^{1/2}}{\bar{v}} \times 100\,\%, \tag{20}$$

where $y(t)$ and $v(t)$ are the lateral location and velocity of the center of a red blood cell at any time instant, $\bar{y}$ and $\bar{v}$ are their mean, and T is the time window over which data is collected. Typically, the RMS and CV are computed over a time in which the cells travel a longitudinal distance of 500–2000 μm. Averages on cell statistics are often done using $>$300 instantaneous measurements.

RMS fluctuations in lateral positions of the red blood cells are shown in Fig. 11 for 40- and 80-μm channels, and for $H_d = 10$–45%. The corresponding tube hematocrits are also mentioned in the figure. The numerical results are compared with the in vivo results (2). In Bishop et al. (2), the velocity and positions of red blood cells were measured in venules (45–75 μm diameter) of the rat spinotrapezius muscle. The numerical results in the figure are shown using various symbols corresponding to different vessel size and hematocrit. For the results of Bishop et al. (2), only the range of their data is indicated. The range of RMS lateral positions reported in Bishop et al. (2) is $\sim$1.5–2.5 μm. In comparison, our numerical results yield a range of 0.5–3 μm. We also observe that the RMS values show a weak dependence on the vessel size. The RMS of fluctuations in the 80-μm channel is higher than that in the 40-μm vessel. While no universal pattern in the RMS fluctuation is observed, the results for $H = 40$ μm and $H_d = 10$ and 20% show that the RMS is higher near the center of the channel, and lower near the wall. At 45% hematocrit, on the contrary, the RMS near the center is lower than that near the wall.

The CV of velocity is plotted in Fig. 12. Here also we compare the simulation results with the in vivo data (2). The simulation results show the similar pattern as observed in the in vivo data: the value of the CV is higher near the wall of

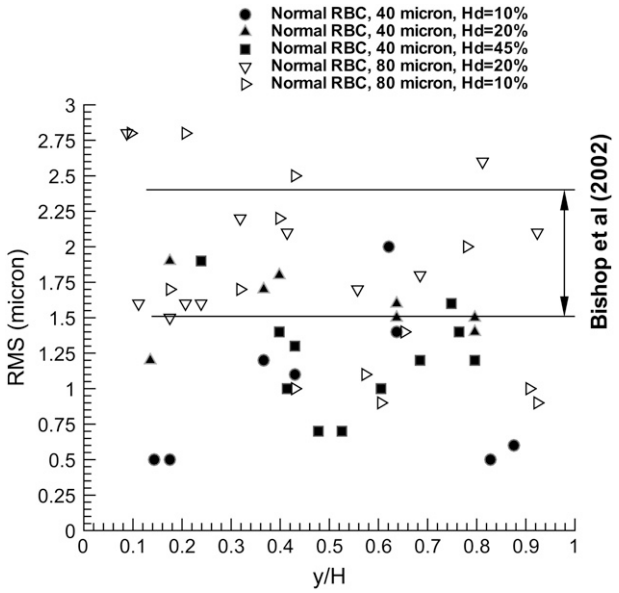

FIGURE 11 RMS fluctuations in lateral position of red blood cells in suspension. Symbols are present numerical simulations. Range of data obtained from the experiments (2) is also shown.

the vessel, and lower near the center. The in vivo data for $H_d = 45\%$ is in the range 12–22%, while the simulation data is in the range 8–16%, and 4–8% for $H_d = 20\%$ and 60%, respectively. The CV decreases with increasing hematocrit due to the reduced tumbling motion and cell-cell interaction in an increasingly close-packed arrangement. In Fig. 12, we also show the CV for the less deformable cells, which yield a higher range of 18–24%. This result is expected based on our earlier observation on the velocity traces for the less deformable RBCs.

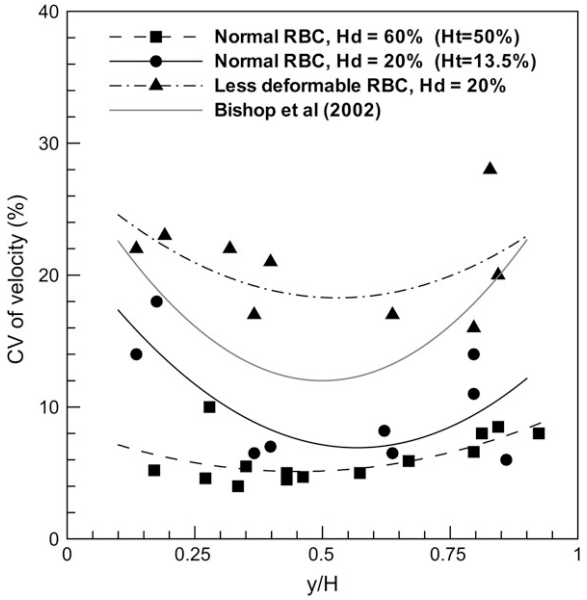

FIGURE 12 Coefficient of variation of red blood cell velocity in a 40-μm channel. Symbols are the present numerical simulations. Thick lines are the best fit through the numerical data. Thin line is the best fit from experimental results (2).

Plug-flow profile

Due to the random motion of the red blood cells, the velocity of the bulk fluid is constantly changing in time. The velocity data over the entire computational domain is stored at frequent intervals during the simulation. They are post-processed to obtain the average velocity profile of blood. The mean velocity profile is obtained by averaging nearly 300 instantaneous measurements, and over all grid points along the x direction.

The time-averaged velocity profiles are shown in Fig. 13 for 20–300-μm channels. The mean velocity (averaged over the cross-section) in dimensional form for various cases is given in Table 2. Also shown is the parabolic profile of the Poiseuille flow, which occurs in pure plasma in absence of the cells for the same pressure gradient. The effect of vessel size, hematocrit, and RBC deformability on the velocity profile is studied here. Consider first the 20-μm channel in Fig. 13 *a*, for which three different discharge hematocrits (20, 45, and 60%) are shown. The values of the tube hematocrits can be found from Table 1. In presence of the RBCs, the plug-flow profile can be seen which is characterized by a nearly constant velocity near the center of the channel. As discharge hematocrit increases, the plug-flow profile becomes more prominent, and extends toward the wall. The maximum centerline velocity rapidly decreases with increasing hematocrit. Also shown is the velocity profile of the blood with less deformable RBCs. Significant reduction is observed in the centerline velocity compared to that with the normal RBCs at the same H_d.

The results for 40- and 80-μm channels are shown in Fig. 13, *b* and *c*, respectively. Again, the effect of hematocrit and cell deformability is shown. Overall similar behavior of the mean velocity is seen here as in the 20-μm channel. The centerline velocity decreases with increasing H_d and decreasing cell deformability. In the 40-μm channel, the centerline velocity in presence of less deformable cells at $H_d = 60\%$ is only 20% of U_{cl}. However, unlike the 20-μm channel, the plug-flow profile is not very prominent for the larger channels. For the 40-μm channel, the profiles are blunt with reduced centerline velocity for $H_d = 20\%$. A plug-flow-like profile is observed only at higher H_d. Same is the case for 80-μm channel; at low H_d, the velocity profile is nearly parabolic, and at higher H_d, it is plug-flow type.

The results for 150- and 300-μm channels are shown in Fig. 13 *d*. The plug-flow profile is clearly absent in these larger vessels. The velocity profiles appear to be nearly parabolic, but with significantly reduced centerline velocity. The numerical observation here is in agreement with the in vivo observation (1,2) and analytical prediction (13). In Bishop et al. (1,2), a fully plug-flow profile was not seen for

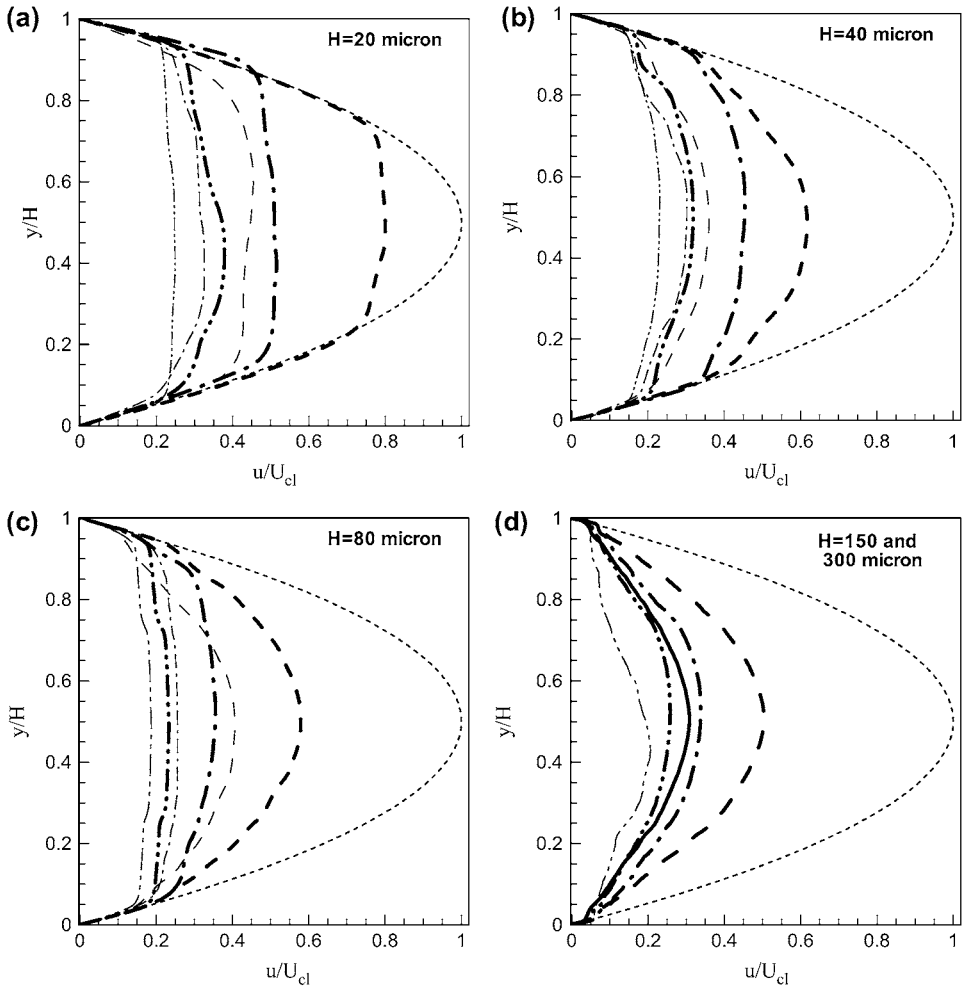

FIGURE 13 Average velocity profile of blood. Dotted line is the parabolic flow. Thick lines represent suspension of normal, deformable RBCs, and thin lines represent suspension of less deformable RBCs. (– – – –) $H_d = 20\%$; (– · – · –) $H_d = 45\%$; and (– · · – · · –) $H_d = 60\%$. In plot *d*, the solid line represents the 300-μm channel at $H_d = 45\%$. The corresponding tube hematocrit can be found from Table 1. Mean velocities are listed in Table 2.

normal blood in 45–75 μm venules at $H_d = 40$–50%. However, the profiles were blunt with reduced centerline velocity as observed here. The in vivo data (1,2) were fit with the equation $u/U_{max} = 1 - (r/R)^K$. Here the exponent $K = 2$ gives a parabola. When $K > 3$, a clear plug-flow profile is obtained. In the experiments (1,2) for normal blood, K lies between 2.1 and 2.2 indicating a blunt profile with reduced centerline velocity. The present numerical data were fit with $u/U_{max} = 1 - (r/R)^K$. It is observed that the numerical data also produce the value of K in the same range as in Bishop et al. (1,2). Sharan and Popel (13) showed that the bluntness of the velocity profile decreases with increasing vessel size and decreasing H_d, in agreement with our numerical results.

Cell-free layer

As discussed earlier, the major factor that contributes to the Fahraeus-Lindqvist effect is the formation of a cell-free layer near the wall of a vessel. Since deformability of the cells is taken into consideration in our computational model, the formation of the cell-free layer can be directly studied. Knowledge about the thickness of the cell-free layer is important, since in many two-phase models of blood flow it is taken as an empirical constant. Note that in our simulations, the red blood cells are initially distributed in a random manner throughout the vessel. As the flow starts, individual cells migrate away from the wall of the channel due to the effect of hydrodynamic shear. However, interaction from the neighboring cells also affects their motion. The cells are repeatedly dispersed toward the wall by such interaction. Eventually a quasi-steady state is reached, and the cell-free layer is formed under a balance of the shear-induced migration and cell-cell interaction.

To obtain the cell-free layer, we first calculate the cell number density distribution across the channel. Following Durlofsky and Brady (38) and Zhou and Pozrikidis (39), we divide the channel into several horizontal zones, count the number of cells in each zone, and normalize by the total number of cells. The instantaneous results are then averaged over time. The interface between the cell-free and cell-rich layers is identified as when the number density reaches zero closest to the wall. The thickness of the cell-free layer as obtained from our simulations is presented in Fig. 14. Here the dimensionless thickness $\delta/(H/2)$, where δ is the dimensional

TABLE 2 Mean blood velocity and shear rate in some representative cases considered in the simulations

Channel size (H, μm)	H_d %	RBC type	Mean velocity (mm/s)	Shear rate (s^{-1})
20	30	Normal	7.5	375
20	45	Normal	5.7	285
20	60	Normal	3.5	175
20	30	Rigid	4.7	235
40	20	Normal	13	325
40	45	Normal	9.5	237
40	60	Normal	7.2	180
40	20	Rigid	7.9	197
40	45	Rigid	6.5	163
40	60	Rigid	6.0	150
80	20	Normal	7.5	94
80	45	Normal	5.0	63
80	60	Normal	3.2	40
80	45	Rigid	3.6	45
150	20	Normal	10.2	68
150	45	Normal	6.5	43
150	45	Rigid	4.9	33
300	45	Normal	12	40

thickness, is plotted. The effect of vessel size, hematocrit, and cell deformability on the cell-free layer thickness is presented. The in vitro data from Bugliarello and Sevilla (4) and the analytical prediction by Sharan and Popel (13) are also presented, and they show good agreement with the numerical data. The dimensionless thickness of the cell-free layer decreases with increasing vessel size, and increasing hematocrit. For a 20-μm channel with $H_d = 20\%$, the cell-free layer covers almost half of the channel. For a 150-μm channel at $H_d = 10\%$, the layer covers only 10% of the cross section. A significant decrease in the cell-free layer is observed for blood with less deformable RBCs. At 20% hematocrit, the layer occupies only ~10% of the cross section in a 40-μm vessel.

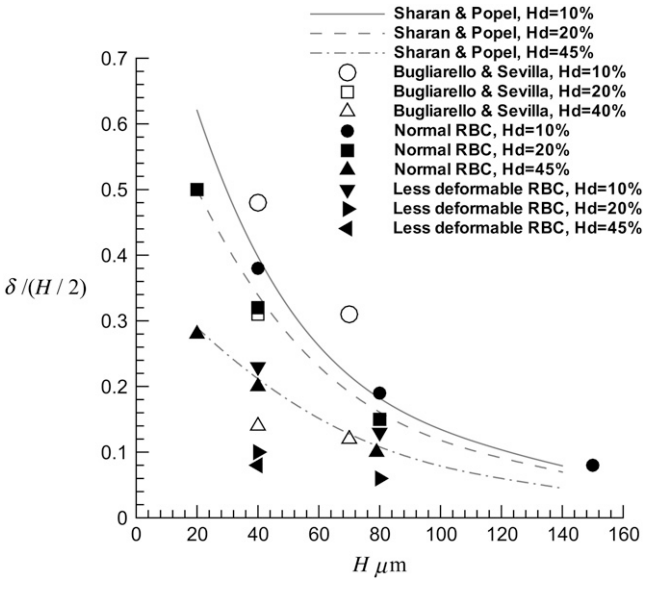

FIGURE 14 Dimensionless cell-free layer $\delta/(H/2)$. Lines are analytical modeling (13), and open symbols are in vitro data (4). Solid symbols are the results from the present numerical simulation.

Apparent viscosity of blood

Since in a microvessel, blood does not behave as a Newtonian fluid, the viscosity of the whole blood is expressed in terms of an apparent viscosity, which is defined as

$$\mu_{app} = \frac{\pi}{128}\frac{\Delta P D^4}{Q L}, \tag{21}$$

where D is the tube diameter, Q is the volumetric flow rate, and $\Delta P/L$ is the pressure gradient. The apparent viscosity depends on the hematocrit, and vessel size. The Fahraeus-Lindqvist effect refers to the decrease in μ_{app} as the vessel size decreases from 500 to 10 μm. In dimensionless form, a relative apparent viscosity is expressed as

$$\mu_{rel} = \frac{\mu_{app}}{\mu_p} = \frac{Q_p}{Q}, \tag{22}$$

where Q_p is the flow rate of the parabolic (Poiseuille) flow in absence of the cells.

The relative apparent viscosity computed from the present simulations is shown in Fig. 15 for the diameter range 20–300 μm, and hematocrit range $H_d = 20$–60%. The results from our simulations are compared with the experimental results given in Pries et al. (3). Based on a comprehensive database for viscosity of blood in narrow glass tubes, Pries et al. (3) gave an empirical expression that takes into account both the effect of vessel diameter and hematocrit. Relative viscosity obtained using their expression is shown in the figure as three solid lines representing $H_d = 20$, 45, and 60%. The numerical results are shown using symbols, which agree very well with the experimental fit of Pries et al. (3). The nonlinear decrease in μ_{rel} as the vessel size drops from 300 to 20 μm is correctly reproduced by our simulations. The increase in μ_{rel} with increasing H_d is also correctly predicted by our simulations. It should be mentioned that μ_{rel} in our simulations appears to be sensitive, though weakly, to the mean flow velocity U_m. In the simulation U_m is not specified a priori, rather it is obtained posteriori. Due to the sensitivity of μ_{rel} to U_m, the actual number of simulations performed is much more than the number of data shown in the figure to obtain a closest match with the empirical fit of Pries et al. (3).

Local variation of μ_{rel}

Flow of blood in microvessels is often described by a two-phase model (13,40,41). In such models, the tube is divided into two regions: a cylindrical core region, and an annular cell-free region. The viscosity of the cell-free layer is usually taken to be equal to that of the plasma. It is noted in Sharan and Popel (13) that the interface between the cell-rich core region and the cell-free layer is not smooth. It is rather rough

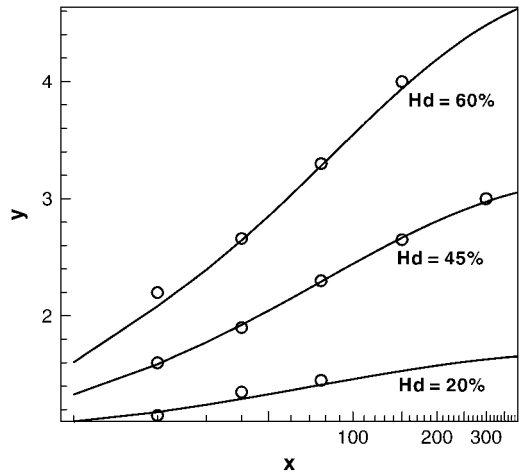

FIGURE 15 The Fahraeus-Lindqvist effect: the relative viscosity of blood as a function of vessel size and discharge hematocrit. The three solid lines represent the empirical expression given in Pries et al. (3) based on in vitro data. The symbols are the data from the present numerical simulation. The tube hematocrit values for a channel size are given in Table 1.

due to the presence of the red blood cells. Sharan and Popel (13) showed that the apparent viscosity in the cell-free layer is higher than the plasma viscosity. They hypothesized that this was due to the rough interface.

In reality, the interface between the core region and the cell-free layer may not be well defined. The RBCs are continuously dispersed toward the wall due to the hydrodynamic interaction with neighboring cells, as it was observed in the present simulations. The interaction also results in heterogeneous cell distribution. Thus the ''effective'' viscosity of blood, defined as $\mu(y)/\mu_p$, is expected to vary across the cross-section of the vessel. Damiano (10) used a semiempirical model in which the effective viscosity is assumed to decrease from a maximum value in the core to a minimum value near the wall. The effective viscosity near the wall corresponds to the plasma viscosity. Subsequently, μPIV measurements (11,12) provided experimental verification on such a ''local'' variation of viscosity across the blood vessel.

The cross-sectional variation of viscosity can be extracted from the present simulations following the approach described in Long et al. (12) and Damiano et al. (11). For a two-dimensional flow of viscous fluid in a channel, with or without cells, the axial momentum equation can be simplified as

$$\frac{\partial \tau_{xy}}{\partial y} = \frac{dP}{dx}, \tag{23}$$

where τ_{xy} is the shear stress. Since the pressure gradient is constant, the above equation can be integrated to give

$$\tau_{xy} = y\frac{dP}{dx}. \tag{24}$$

The constitutive relationship between the local shear stress and rate of strain can then be invoked as

$$\tau_{xy} = \dot{\gamma}(y)\mu(y), \tag{25}$$

where $\dot{\gamma}(y)$ and $\mu(y)$ are the shear rate and blood viscosity that vary along the cross-section of the channel. The above two relations give

$$\mu(y) = \frac{y}{\dot{\gamma}}\frac{dP}{dx}, \tag{26}$$

which is used to obtain $\mu(y)$ in our simulations.

Simulation results on $\mu(y)/\mu_p$ are shown in Fig. 16. First we note that $\mu(y)$ is equal to the plasma viscosity very close to the wall, and it is higher than the plasma viscosity near the center of the vessel. This behavior is in agreement with the assumptions made in the macroscopic two-phase models of blood as mentioned above. However, over the cross section of the vessel, $\mu(y)$ shows a strongly nonmonotonic behavior, unlike the monotonic variation assumed in Damiano (10). Most strikingly, $\mu(y)$ shows a strong peak near the wall. The exact location and magnitude of the peak depends on the vessel size and hematocrit. For a 40-μm vessel at $H_d = 10\%$, the peak occurs at $y/H = 0.65$ with a magnitude of $\mu(y)/\mu_p = 2.5$. The peak moves further toward the wall and the magnitude increases to $\mu(y)/\mu_p = 19$ as the hematocrit increases to 60%.

Earlier in Fig. 14 we presented the thickness of the cell-free layer obtained from our simulations. These results can be used to obtain the location of the interface between the cell-free layer and the cell-rich core region. The location of the peak in $\mu(y)$ as observed in Fig. 16 matches with the location of the interface between the cell-free layer and the cell-rich core region. Thus our results suggest that the local viscosity of blood is the maximum at the interface. This

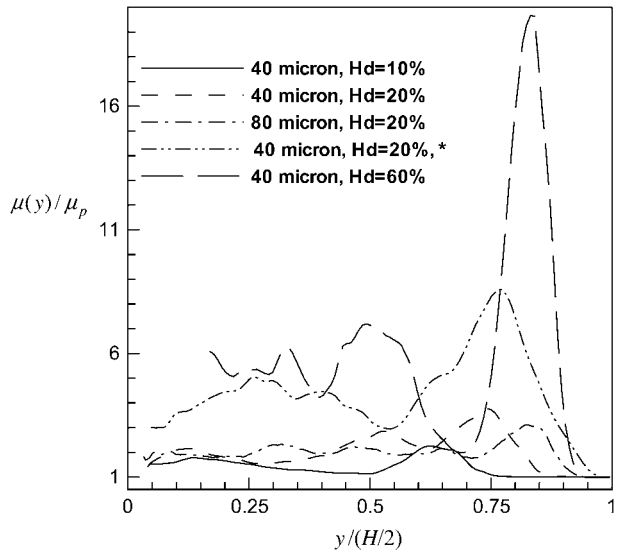

FIGURE 16 The variation of local effective viscosity along the wall-normal direction across the channel. Here $y/(H/2) = 0$ is the center of the channel, and $y/(H/2) = 1$ is the wall. The asterisk denotes less deformable cells. All other cases are for normal cells.

result is consistent with the proposition made in Sharan and Popel (13), that the roughness of the interface results in a higher local viscosity.

Fig. 16 also shows that as the hematocrit increases, the location of the peak moves toward the wall. It is because the cell-free layer shrinks, and the interface moves toward the wall as H_d increases. The increase in H_d also results in an increase in the peak magnitude of $\mu(y)$. It is because the number of RBCs at the interface increases with increasing H_d resulting in increased roughness of the interface, and hence higher local dissipation.

From the present results, one can also estimate the effective viscosity of the cell-free layer $\mu_{rel,\,cfl}$ and that of the core region $\mu_{rel,\,core}$. We note that for a given pressure drop, using Eq. 26 one can write

$$\mu_{rel}(y) = \frac{\mu(y)}{\mu_p} = \frac{\dot{\gamma}_p(y)}{\dot{\gamma}(i)}, \tag{27}$$

where $\mu_{rel}(y)$ is the local variation of relative viscosity across the channel, and $\dot{\gamma}_p(y)$ is the shear rate variation across the channel in a Poiseuille flow. The above equation for local viscosity can be integrated across the channel and then scaled by the channel size to give the relative apparent viscosity of whole blood. This method can be viewed as an alternative way to find the apparent viscosity when the local variation of viscosity is known. The result is of course the same as the one obtained directly from Eqs. 21 and 22. Following this argument, one can say that if the integration of Eq. 26 is performed over a section of the channel, then the result would represent the contribution of that section to the effective viscosity. Thus we compute the relative viscosities of the core and cell-free layers as

$$\mu_{rel,core} = \int_0^{\lambda} \mu_{rel}(y^*)dy^*, \tag{28}$$

$$\mu_{rel,cfl} = \int_{\lambda}^{1} \mu_{rel}(y^*)dy^*, \tag{29}$$

where $\lambda = 1 - \delta/(H/2)$ and $y^* = y/H$. The method is appropriate in our case since the local variation of viscosity across the channel is known from the simulation data (Fig. 16). These results are shown in Table 3 for a 40-μm channel at various H_d. Also shown are the estimates given in Sharan and Popel (13). First we note that $\mu_{rel,\,cfl}$ is >1, implying that the effective viscosity in the cell-free layer is higher than the plasma viscosity, as mentioned in Sharan and Popel (13). In general, our results show that $\mu_{rel,\,cfl}$ is $<\mu_{rel,\,core}$. However, the numerical results give higher values of $\mu_{rel,\,cfl}$ than those predicted by Sharan and Popel (13).

TABLE 3 Core versus cell-free layer viscosity for 40-μm channel

H_D%	μ_{rel}	$\mu_{rel,\,core}$ (Present)	$\mu_{rel,\,cfl}$ (Present)	$\mu_{rel,\,cfl}$ (Sharan and Popel (13))
10	1.15	1.18	1.02	—
20	1.4	1.42	1.35	1.25
60	2.66	2.7	2.03	1.35

DISCUSSION AND CONCLUSION

This article presents two-dimensional numerical simulation of blood flow in 20–300-μm channels taking into consideration the particulate nature of blood. The objective is to study the characteristics of the motion of individual red blood cell in suspension, and how the collective motion of many cells leads to the development of the cell free layer, plug-flow profile, the apparent blood viscosity, and the Fahraeus-Lindqvist effect. The numerical model is based on the immersed boundary method, and the red blood cells are modeled as liquid capsules of biconcave shapes. The cells in our model are free to deform in an external shear flow. As many as 2500 cells are considered in the simulation. Computational simulation of suspension of multiple deformable particles is a major challenge. To the best of our knowledge, this article presents the first computational study that takes into consideration such a large number of cells and the cell deformation. Though two-dimensional in nature, the present simulation can successfully predict many aspects of the RBC motion and blood flow in microvessels in vitro. The model also allows us to study the effect of the loss of cell deformability, as it is the case in many blood disorders, such as sickle cell anemia.

First, we present results on the dynamics of red blood cells in dilute suspension, and discuss the tank-treading and tumbling motion, and the lateral migration. The motion of a single, isolated red blood cell in a 40-μm channel is studied at varying degree of cell deformation. A normal, easily deformable RBC is observed to undergo simultaneous tumbling and tank-treading motion. A less deformable RBC, on the contrary, undergoes only tumbling motion. A normal cell repeatedly attains biconcave and elliptic shapes during its motion at moderate shear rates. At high shear rates the RBC loses its biconcave shape, and attains an elliptic shape oriented at an angle with the flow. The RBC is observed to migrate laterally away from the wall and toward the center of the channel. The rate of migration depends on the deformability of the cell; a normal, deformable cell migrates faster than a less deformable cell. The rate of migration also depends on the instantaneous location of the cell. It is higher when the RBC is located near the wall, and it decreases as the cell moves closer to the center. The numerical results on the isolated RBC correspond to the motion of a cell in a dilute suspension, and are in agreement with the experimental observation (14).

We then consider the motion of a suspension of red blood cells flowing through 20–300-μm channels at discharge hematocrit 10–60%. The number of RBCs considered in a typical simulation varies from 5 to 2500. The motion of

individual cells in the suspension depends on the channel size, hematocrit, and cell deformability. In small vessels, the cells near the center assume a slipper shape. As the vessel size increases, the slipper shape is no longer seen. In large vessels, the cells near the wall deform significantly, while those near the center deform less. Normal cells in a suspension do not show a significant tumbling motion. Rather, they are mostly aligned at a regular angle with the flow. Less deformable cells, on the contrary, show evidence of tumbling resulting in increased dispersion of the cells and random alignment. Tumbling motion is suppressed as the discharge hematocrit increases.

Individual RBC exhibits fluctuations in its position and velocity. At low hematocrit, when cell-cell interaction is less, fluctuations arise due to the tumbling motion of individual cells, which increase with increasing rigidity. As hematocrit increases, fluctuations increase due to increased cell-cell interaction. Upon further increase in hematocrit, fluctuations are suppressed, as the close-packed cells move in a stacklike manner. RMS and CV of fluctuations obtained in the simulations are in good agreement with the in vivo measurement (2).

The effect of vessel size, hematocrit, and cell deformability on the plug-flow velocity profile is studied. The presence of the cells significantly reduces the centerline velocity compared to the Poiseuille flow. A clear plug-flow profile is seen for 20-μm vessels, whereas a parabolic, but blunt, profile with a strongly reduced centerline velocity is observed for vessels of larger size. The bluntness of the velocity profile reduces with increasing vessel size, and decreasing hematocrit, in agreement with Sharan and Popel (13). An empirical fit of the numerical data with the equation $u/U_{\max} = 1 - (y/(H/2))^K$ yields the value of K in the range 2.1–2.2, similar to that in Bishop et al. (2), for 40–300-μm vessels.

The inclusion of cell deformation in the numerical model allows us to study the formation of the cell-free layer near the wall of a vessel. We observe that RBCs in a dense suspension, unlike those in a dilute suspension, do not migrate continuously toward the center of the channel. The migration is strongly inhibited by cell-cell interaction as the hematocrit increases. A cell-free layer is formed under a balance between the lateral migration of individual cell, and the dispersive effect of cell-cell interaction. The ratio of the thickness of the cell-free layer to the vessel size decreases with increasing vessel size, discharge hematocrit, and cell deformability. The numerical data is in good agreement with the analytical prediction (13), and experimental results (4).

The apparent viscosity of blood is computed from the simulations as a function of vessel size (20–300 μm) and discharge hematocrit (20–60%). It is in agreement with the empirical correlation (3) based on in vitro measurements. The numerical results correctly predict the Fahraeus-Lindqvist effect. We also study the local variation of the effective viscosity of blood as a function of the wall-normal direction across the vessel. The effective viscosity is shown to vary in a nonmonotonic manner across the vessel. It is equal to the plasma viscosity close to the wall, and higher near the center. However, it sharply increases at the edge of the cell-free layer. The result supports the proposition of Sharan and Popel (13) that the interface between the cell-free region and the cell-rich region results in an increased energy dissipation. As in Sharan and Popel (13), we observe that the effective viscosity of the cell-free layer is higher than the plasma viscosity. However, the numerical result gives higher values of cell-free layer effective viscosity than those given in Sharan and Popel (13).

It should be mentioned that there are several limitations to the simulations presented here. First, the simulations are two-dimensional, while the actual problem of RBC deformation and cell-cell interaction is inherently three-dimensional. Also, Eq. 18 is based on empirical fit to the in vitro data, and is not strictly applicable to the two-dimensional case. For a given discharge hematocrit, the tube hematocrit depends on the velocity profile and the distribution of red blood cells. Thus the results presented here must be taken cautiously while comparing quantitatively with experiments. Nevertheless, the article is a significant improvement in computational modeling of blood flow in small vessels in comparison to the previous studies (22), which considered two-dimensional simulations of rigid ellipsoids as models for RBC, and up to a few tens of cells in number. The present study takes the mesoscale simulation of blood flow to the next level of improvement by considering the deformability of the RBC using a simple model and $O(10^3)$ cells in number. A fully three-dimensional simulation of multiple RBC motion is computationally very challenging, and is not forthcoming.

The second limitation of the RBC model is that it does not include the viscous resistance of the cell membrane. The viscosity μ_m of the RBC membrane is $\sim$0.001 dyn s/cm (42). Two dimensionless parameters can be formed using μ_m. First is $\mu_m/\mu_p a$, which is $\sim$100 for a normal RBC. The second parameter, also called Deborah number (43,44), is defined as $\mu_m\dot{\gamma}/E_s$. For the present case, the Deborah number is more relevant than the first parameter, as it represents the ratio of the viscous resistance to the elastic resistance of the cell membrane. For a shear rate in the range 1–100 s^{-1}, this number ranges from 0.01 to 1, implying that the viscous resistance is less or of the order of, but not significantly higher than, the elastic resistance. In an earlier article (32), we have performed numerical experiments using one and two RBCs by including viscoelasticity in our model. This requires an additional body force term, like **F** in Eq. 2, in the Navier-Stokes equation. Our previous simulations suggest that inclusion of viscoelasticity does not significantly alter the results for the current parametric range of interest (32).

The agreement between the computational and experimental results for apparent viscosity is rather remarkable and probably coincidental given the two-dimensional nature of the simulations, while the predicted values of the cell-free

layer are smaller than those reported in the experiment of Bugliarello and Sevilla. We note that while there is abundant experimental data available on the apparent viscosity of blood in narrow tubes, relatively fewer articles report data on the cell-free layer thickness. The error bar for the experimental data of Bugliarello and Sevilla is rather large. The impact of the cell-free layer thickness is different in a tube flow than in a two-dimensional channel. The relative viscosity based on the two-layer model of blood flow in a tube is given by (6)

$$\mu_{\mathrm{rel}} = \frac{1}{1 - \lambda^4(1 - \mu_{\mathrm{p}}/\mu_{\mathrm{core}})}. \tag{30}$$

For a two-dimensional channel, the exponent of λ is 3 instead of 4. It should also be mentioned that the cell-free layer viscosity may not be equal to the plasma viscosity, as our simulations show. Further, the cell-free layer viscosity and the core viscosity may not be identical in tube and channel flows, and hence they may contribute differently in circular and rectangular geometry.

Further, the neo-Hookean law used to represent the RBC membrane in our model allows continuous stretching of the membrane as the shear rate increases. The real membrane behaves as a nearly incompressible surface, and the RBC deforms without area stretching. Thus above a shear rate, the cells are maximally deformed, and the effective viscosity is independent of the shear rate. Our two-dimensional model does not capture this behavior as the cells continue to elongate with increasing shear rate. Alternatively, one can consider the variation of effective viscosity with increasing tube diameter. The effective viscosity is independent of the tube diameter beyond $\sim$600 μm. Simulating blood flow in vessels of this size using our model is computationally very expensive. However, the asymptotic trend in effective viscosity as shown in Fig. 15 suggests that our model would correctly predict that the effective viscosity is independent of the channel size for larger channels.

The new contribution of the article is that it takes the mesoscale simulation of blood flow to the next step by including deformability of the cells and a large number of them. Specific new results include the effect of less deformable (e.g., sickle) RBC on the statistics of the motion, and cell-free layer thickness, apart from the local variation of the viscosity. The simulation tool can be applied to a number of other problems related to microcirculation. One example is margination, rolling, and adhesion dynamics of white blood cells under varying hematocrit and channel size in presence of normal and sickle RBC suspension. The model can also be extended to consider aggregation of red blood cells (32), dispersion of platelets, solute, and drug particles by random motion of the RBCs.

We greatly acknowledge computational support on the IBM p690 at the National Center for Supercomputing Applications at Urbana, Illinois.

REFERENCES

1. Bishop, J. J., P. Nance, A. S. Popel, M. Intaglietta, and P. C. Johnson. 2001. Effect of erythrocyte aggregation on velocity profiles in venules. *Am. J. Physiol.* 280:H222–H236.
2. Bishop, J. J., A. S. Popel, M. Intaglietta, and P. C. Johnson. 2002. Effect of aggregation and shear rate on the dispersion of red blood cells flowing in venules. *Am. J. Physiol.* 283:H1985–H1996.
3. Pries, A. R., D. Neuhaus, and P. Gaehtgens. 1992. Blood viscosity in tube flow: dependence on diameter. *Am. J. Physiol.* 263:H1770–H1778.
4. Bugliarello, G., and J. Sevilla. 1970. Velocity distribution and other characteristics of steady and pulsatile blood flow in fine glass tubes. *Biorheology.* 7:85–107.
5. Popel, A. S., and P. C. Johnson. 2005. Microcirculation and hemorheology. *Annu. Rev. Fluid Mech.* 37:43–69.
6. Secomb, T. W. 2003. Mechanics of red blood cells and blood flow in microcirculation. *In* Modeling and Simulation of Capsules and Biological Cells. C. Pozrikidis, editor. Chapman and Hall/CRC, New York.
7. Fahraeus, R., and T. Lindqvist. 1931. The viscosity of blood in narrow capillary tubes. *Am. J. Physiol.* 96:562–568.
8. Goldsmith, H. L., G. R. Cokelet, and P. Gaehtgens. 1989. Robin Fahraeus: evolution of his concepts in cardiovascular physiology. *Am. J. Physiol.* 257:H1005.
9. Cokelet, G. R., and H. L. Goldsmith. 1991. Decreased hydrodynamic resistance in the two-phase flow of blood through small vertical tubes at low flow rates. *Circ. Res.* 68:1–17.
10. Damiano, E. R. 1998. Blood flow in microvessels lined with a poroelastic wall layer. *In* Poromechanics. J. F. Thimus, Y. Abousleiman, A. H. D. Chang, O. Coussy, and E. Detournay, editors. A. A. Balkema, Rotterdam, The Netherlands.
11. Damiano, E. R., D. S. Long, and M. L. Smith. 2004. Estimation of viscosity profiles using velocimetry data from parallel flows of linearly viscous fluids: application to microvascular hemodynamics. *J. Fluid Mech.* 512:1–19.
12. Long, D. S., M. L. Smith, A. R. Pries, K. Ley, and E. R. Damiano. 2004. Microviscometry reveals reduced blood viscosity and altered shear rate and shear stress profiles in microvessels after hemodilution. *Proc. Natl. Acad. Sci. USA.* 101:10060–10065.
13. Sharan, M., and A. S. Popel. 2001. A two-phase model for flow of blood in narrow tubes with increased effective viscosity near the wall. *Biorheology.* 38:415–428.
14. Goldsmith, H. L. 1971. Red cell motions and wall interactions in tube flow. *Fed. Proc.* 30:1578–1590.
15. Happel, J., and H. Brenner. 1983. Low Reynolds Number Hydrodynamics. Kluwer, New York.
16. Reference deleted in proof.
17. Secomb, T. W., R. Skalak, N. Ozkaya, and J. F. Gross. 1986. Flow of axisymmetric red blood cells in narrow capillaries. *J. Fluid Mech.* 163:405–423.
18. Pozrikidis, C. 2003. Numerical simulation of the flow-induced deformation of red blood cells. *Ann. Biomed. Eng.* 31:1194–1205.
19. Damiano, E. R. 1998a. The effect of the endothelial-cell glycocalyx on the motion of red blood cells through capillaries. *Microvasc. Res.* 55:77–91.
20. Eggleton, C. D., and A. S. Popel. 1998. Large deformation of red blood cell ghosts in a simple shear flow. *Phys. Fluids.* 10:1834–1845.
21. Hsu, R., and T. W. Secomb. 1989. Motion of nonaxisymmetric red blood cells in cylindrical capillaries. *J. Biomech. Eng.* 111:147–151.
22. Sun, C., and L. L. Munn. 2005. Particulate nature of blood determines macroscopic rheology: a 2D lattice-Boltzmann analysis. *Biophys. J.* 88:1635–1645.
23. Peskin, C. S. 1977. Numerical analysis of blood flow in the heart. *J. Comput. Phys.* 25:220–233.
24. Unverdi, S. O., and G. Tryggvason. 1992. A front-tracking method for viscous, incompressible multi-fluid flows. *J. Comput. Phys.* 100:25–37.

25. Tryggvason, G., B. Bunner, A. Esmaeeli, N. Al-Rawahi, W. Tauber, J. Han, S. Nas, and Y. Jan. 2001. A front tracking method for the computations of multiphase flow. *J. Comput. Phys.* 169:708–759.

26. Fung, Y. C. 1993. Biomechanics: Mechanical Properties of Living Tissues, 2nd Ed. Springer, New York.

27. Skalak, R., A. Tozeren, P. R. Zarda, and S. Chien. 1973. Strain energy function of red blood cell membranes. *Biophys. J.* 13:245–264.

28. Evans, E. A., and R. Skalak. 1980. Mechanics and Thermodynamics of Biomembranes. CRC, Boca Raton, FL.

29. Barthes-Biesel, D., A. Diaz, and E. Dhenin. 2002. Effect of constitutive laws for two-dimensional membranes on flow-induced capsule deformation. *J. Fluid Mech.* 460:211–222.

30. Pozrikidis, C. 2001. Effect of membrane bending stiffness on the deformation of capsules in simple shear flow. *J. Fluid Mech.* 440: 269–291.

31. Bagchi, P., and S. Balachandar. 2002. Steady planar straining flow past a rigid sphere at moderate Reynolds numbers. *J. Fluid Mech.* 466:365–407.

32. Bagchi, P., P. C. Johnson, and A. S. Popel. 2005. Computational fluid dynamic simulation of aggregation of deformable cells in shear flow. *J. Biomechanical Eng.* 127:1070–1080.

33. Mortazavi, S., and G. Tryggvason. 2000. A numerical study of the motion of drops in Poiseuille flow. Part 1. Lateral migration of one drop. *J. Fluid Mech.* 411:325–350.

34. Fischer, T. M., M. Stohr-Liesen, and H. Schmid-Schonbein. 1978. The red cell as a fluid droplet: tank-tread-like motion of the human erythrocyte membrane in shear flow. *Science.* 202:894–896.

35. Keller, S. R., and R. Skalak. 1982. Motion of a tank-treading ellipsoidal particle in a shear flow. *J. Fluid Mech.* 120:27–47.

36. Ramanujan, S., and C. Pozrikidis. 1998. Deformation of liquid capsules enclosed by elastic membranes in simple shear flow: large deformations and the effect of fluid viscosities. *J. Fluid Mech.* 361: 117–143.

37. Coulliette, C., and C. Pozrikidis. 1998. Motion of an array of drops through a cylindrical tube. *J. Fluid Mech.* 358:1–28.

38. Durlofsky, L. J., and J. K. Brady. 1989. Dynamic simulation of bounded suspension of hydrodynamically interacting spheres. *J. Fluid Mech.* 200:39–67.

39. Zhou, H., and C. Pozrikidis. 1993. The flow of ordered and random suspension of two-dimensional drops in a channel. *J. Fluid Mech.* 255:103–127.

40. Nair, P. K., J. D. Hellums, and J. S. Olson. 1989. Prediction of oxygen transport rates in blood flowing in large capillaries. *Microvasc. Res.* 38:269–285.

41. Seshadri, V., and M. Y. Jaffrin. 1977. Anomalous effects in blood flow through narrow tubes: a model. *INSERM Euromech.* 92:265–282.

42. Evans, E. A., and R. M. Hochmuth. 1976. Membrane viscoelasticity. *Biophys. J.* 16:1–11.

43. Barthes-Biesel, D. 1991. Role of interfacial properties on the motion and deformation of capsules in shear flow. *Physica A.* 172:103–124.

44. Barthes-Biesel, D., and H. Sgaier. 1985. Role of membrane viscosity in the orientation and deformation of a spherical capsule suspended in shear flow. *J. Fluid Mech.* 160:119–136.